Spring 2014

Characterization Of Thermal And Mechanical Properties Of Porous Material For Electronic Cooling Applications

Ninad Tushar Trifale
Purdue University

PURDUE UNIVERSITY
GRADUATE SCHOOL
Thesis/Dissertation Acceptance

This is to certify that the thesis/dissertation prepared

By Ninad Tushar Trifale

Entitled

CHARACTERIZATION OF THERMAL AND MECHANICAL PROPERTIES OF POROUS MATERIAL FOR ELECTRONIC COOLING APPLICATIONS

For the degree of Master of Science in Mechanical Engineering

Is approved by the final examining committee:

Dr. Eric Nauman

Dr. Kazuaki Yazawa

Dr. Timothy Fisher

To the best of my knowledge and as understood by the student in the *Thesis/Dissertation Agreement. Publication Delay, and Certification/Disclaimer (Graduate School Form 32)*, this thesis/dissertation adheres to the provisions of Purdue University's "Policy on Integrity in Research" and the use of copyrighted material.

Dr. Eric Nauman

Approved by Major Professor(s): _____

_____

Approved by: Dr. David Anderson 04/28/2014

Head of the Department Graduate Program Date

CHARACTERIZATION OF THERMAL AND MECHANICAL PROPERTIES OF POROUS MATERIAL FOR ELECTRONIC COOLING APPLICATIONS

A Thesis

Submitted to the Faculty

of

Purdue University

by

Ninad T Trifale

In Partial Fulfillment of the

Requirements for the Degree

of

Master of Science in Mechanical Engineering

May 2014

Purdue University

West Lafayette, Indiana

ACKNOWLEDGEMENTS

I would like to thank with Dr. Eric Nauman and Dr. Kazuaki Yazawa for the timely support and necessary guidance. Their insights and patient counsel has been crucial for this study.

I want to thank Dr. Timothy Fisher for his support on my committee.

I deeply appreciate support for this work from the Cooling Technologies Research Center (CTRC), an NSF Industry/University Cooperative Research Center at Purdue University, to provide for use of the thermal contact conductance setup.

I want to thank Dr. S. K. Vytla and Mr. Y. Ando (Cradle North America) for providing a 3D CFD conjugate heat transfer simulation to correlate with the current study.

TABLE OF CONTENTS

Page

Page

LIST OF TABLES

Table Page

Appendix Table

LIST OF FIGURES

Figure Page

Figure Page

Figure Page

NOMENCLATURE

SYMBOL	UNIT	DESCRIPTION
a	m	cube edge length
A	m^2	area
B	m	base plate height
d	m	pore size
d		dimensionless strut radius
e		dimensionless cube edge length
E	Pa	Young's Modulus
H	m	total height of the heat sink
h	W/m2K	heat transfer coefficient
K	m2	permeability
k	W/mK	thermal Conductivity
L	m	edge length tetrakaidecahedron
L	m	length along flow direction
m	kg	mass

SYMBOL	UNIT	DESCRIPTION
n		number of struts in contact
p		radius
P	N/m2	pressure
P	N	Force
Q	J	total heat transfer
q	Kg m/s	flow rate
R		relative Density
Rek		specific Reynolds number
r	m	radius of void sphere
r	m	radius of strut cylinder
s	m	center distance in voids
T	K	temperature
t	m	thickness
U	m/s	velocity
V	m3	volume
W	J	work
w	m	width of contact area
x	m	length

Greek Symbols

SYMBOL	UNIT	DESCRIPTION
μ	Ns/m2	dynamic viscosity
ε		porosity
θ		dimensionless temperature
ρ		density kg/m3
σ	m2/m3	specific surface area
δ	m	deformation
δ’	m	length of strut in contact

Subscripts

SYMBOL	DESCRIPTION
ap	apparent
b	base
cond	conduction
conv	convection
eff	effective
f	fluid
fm	foam
in	inlet
L	long length

SYMBOL	DESCRIPTION
s	solid
sf	surface
t	total

ABSTRACT

Trifale, Ninad T. M.S.M.E., Purdue University, May 2014. Characterization of Thermal and Mechanical Properties of Porous Material for Electronics Cooling Applications. Major Professor: Dr. Eric Nauman, School of Mechanical Engineering.

Metal foams are considered beneficial for several applications because of its significantly large surface area for a given volume. Foams form a high thermal conductive network in a thermal interface for electro cooling applications. The porous structures are relatively compliant and can provide for a better contact and thereby have a lower thermal resistance. Porous heat sinks made of aluminum foam have been well studied in the past. It is not only cost effective due to the unique production process, but also attractive for the theoretical modeling study to determine the performance. A study on the thermal and mechanical characterization of metal foams is presented. Metal foams are analyzed as viable thermal interfaces and heat sinks focusing on the electronics cooling applications. Generalized analytic models are developed to predict intrinsic thermal resistance as well as the contact thermal resistance defined by micro-deformation at the contact surfaces. Properties of porous structure as an effect of the characteristic geometric parameters are evaluated. Effective Young's modulus, effective thermal conductivity, Coefficient of thermal expansion, and surface contact, area for deformation are evaluated through analytic models and simulations. Experiments are also carried out in accordance to the

ASTM D5470 standard for determining the total thermal resistance. The results verify the calculation from the model in intrinsic thermal conductivity of the foam as well as the constriction resistance to the actual area of contact. The bulk thermal resistance -contact resistance trade-off for thermal interface applications and pressure drop- heat transfer trade-off for heat sink applications are studied. An optimum value of porosity and pore size is found out for thermal interface and heat sink applications individually.

CHAPTER 1. INTRODUCTION

1.1 Introduction

The current trends for exponential increase in the performance capabilities of the integrated circuits and processors require better heat dissipation techniques which not only have adequate performance but are also economical and energy friendly from a system integration perspective. Over the past decade the reduction of chip size and increase in performance has resulted in a large power density 50 W/cm^2. Often thermal management of these chips becomes a limiting factor for design and hence there is a need to develop better cooling solutions. There is a challenge to dissipate this heat in order to ensure smooth performance of the chip and enhance the reliability of the package. This chapter provides a background on existing thermal management techniques (thermal interface materials, heat sinks) and a background on use of porous structure material which is the focus of this study.

1.2 Thermal Interface Materials

Conduction across two interfaces such as chip and heat sink is critical for heat dissipation. A surface to surface contact usually creates a large contact resistance which can be attributed to the roughness of the two surfaces and reduced actual area of contact. In

applications concerning heat transfer across interfaces, thermal resistance can be a useful parameter to characterize the performance. Thermal resistance is a measure of the resistance to heat flow through the material, or in this case interface. Mathematically it can be defined as:

$$R = \frac{T_{hot} - T_{cold}}{Q'} \quad . \tag{1}$$

For conduction across any interface, the contact resistance is the dominant factor in determining the net heat flow. The reduced actual contact area, which is about 1-2% of the apparent area of contact [1], gives rise to the contact resistance. A small increase in the contact conductance can substantially affect the efficiency of the system to dissipate heat.

Thermal interface materials are used to reduce this contact resistance between any two surfaces and promote conduction through the interface. They are typically used between the chip- heat spreader interfaces (TIM1) as well as between the heat spreader – heat sink interface (TIM2). Figure 1.1 shows the typical assembly for heat dissipation from a chip. The TIM1 is on top of the chip. The other side of TIM1 is in contact with the heat spreader. TIM1 are usually thinner than TIM2 and are required to have a very high conductivity and compliance. TIM2 comes on top of the heat spreader and enhances heat conduction through to the heat sink. The current work focuses on use of aluminum porous structure as a potential TIM2 material.

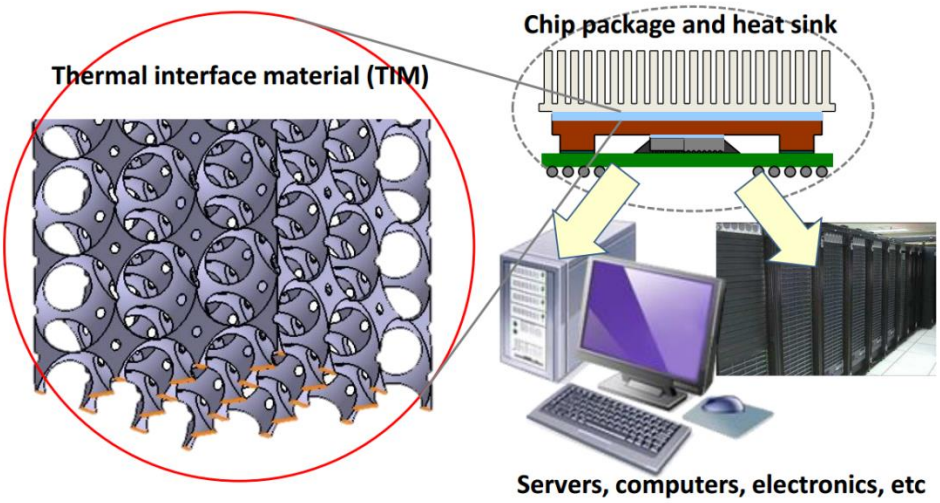

Figure 1.1. Chip packaging, porous structure and applications.

Thermal interface materials have three components of resistances Figure 1.2, two contact resistances at either surfaces and a bulk thermal resistance which is dependent on the bulk conductivity and the thickness of the material. In most cases the contact resistance is the dominant factor for the overall thermal resistance. It is advantageous to study and focus on the contact resistance as there is a lot of potential to enhance conductivity by reducing it. As will be discussed further, there are distinct trade-offs observed between the contact resistance and the bulk resistance in most cases.

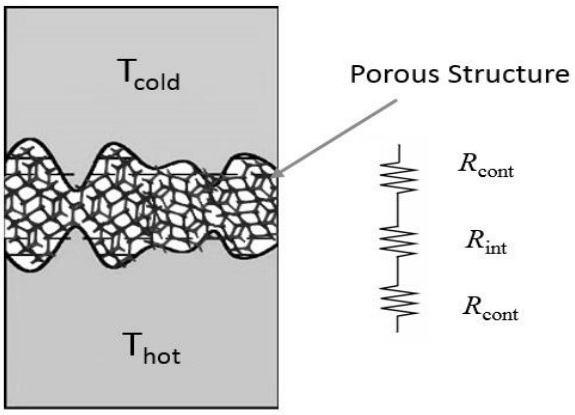

Figure 1.2. Thermal resistance components.

Over the years there has been a lot study on different thermal interface materials. Recent work has been targeted at developing carbon structures such as CNT [2]-[5] and graphene [6],[11]since these structures have extremely high thermal conductivity (~3000 W/mK). The effectiveness of these TIMs is restricted due to relatively high contact resistances and there have been multiple studies to create a better bonding between the substrate and CNTs/graphene [3]. Additionally there have been studies on thermal interfaces with carbon nanotube inclusions [7]. It was found that there exists an optimum value for the volume fraction of such inclusions. There are other possible solutions such as thermal greases, metal pads, polymers, phase change materials, low melting temperature alloys etc. But all of them have specific advantages and disadvantages. Additionally unconventional materials have also been considered for possible thermal interface material applications- sodium silicate based [8], gallium based [9], aluminum oxide based [10] – to name a few. There has been in general extensive research in this field which is also fueled by the ever increasing requirement for better products.

This study effectively aims at developing the foundation for creating generalized models for porous material, so that going forward, the advantages of thermal grease and metal pads can be effectively combined to result in a better performance with the right choice of material and geometry.

Table 1: Comparison of different TIMs [11][14].

TIM	Resistance ($kcm^{2/W}$)	Advantages	Disadvantages
Grease	0.2-1	• High effective thermal conductivity • Low thermal resistance as a result of thin Joint with minimal attach pressure • Ability to fill interstices and reduce interstitial air • No curing is required • Delamination is not an issue • Low cost • Do not require shape cutting	• Not manufacturing friendly • Pump-out as a result of thermal cycling • Can dry-out overtime • Can be messy to handle • Difficult to control thickness (uniform application) • Usually do not provide electrical insulation • Requires curing
Pads	1-3	• Can be handled more easily • Not messy • Thermal compound is distributed uniformly on thermal pads • Conforms to surface irregularity before cure • Less likely to pump out or leak out of the interface • Resists humidity and can equally act as a vibration damper • Can be easily cut to required size • Can be fitted with a thin layer of pressure-sensitive adhesive (PSA) to enhance adhesion at the interfaces • Can be compressed to absorb tolerance variation in assemblies	• Thermal conductivity is lower than that of grease • Delamination can be an issue • Do not have free flow movement • Permanent clamping required • More expensive than grease • Require high contact pressures to conform to mating surfaces • Increased thermal resistance as a result of inadequate pressure
PCMs	0.3-0.7	• Increased stability and less vulnerability to pump-out • Easier to handle compared to greases • No cure is required • Delamination is not an issue • No dry-out • Ability to conform to profiles of mating surfaces	• Lower thermal conductivity than greases • Limited thermal performance as a result of ‘‘phase-change’’ (polymers and filler combinations) trade off • Surface resistance can be greater than greases although this can be reduced by thermal pretreatment • Compressive force required which can cause mechanical stresses • Additional barrier is required for electrical isolation

Table 1.1: Continued.

Gels	0.4-0.8	• Offer properties of solid and liquid • Good wetting capabilities • Able to surround irregular shapes • Adhere to complex surface features • Good shape retention • High cohesive strength • High temperature stability • No pump out or migration concerns	• Cure process required • Lower thermal conductivity compared to grease • Delamination can be a concern
Thermal Adhesives	0.15-1	• No pump out • No migration • Do not require mechanical clamp • Conform to surface irregularity before cure	• Cure process required • CTE variation induced stress is a concern since • cured epoxies have modulus • Delamination post reliability test is a concern

As mentioned before, the contact resistance is more dominant of the two resistance, so naturally, having a larger actual contact area is the logical way to enhance the overall conductance. More mechanical compliance will result in a larger contact area and subsequently, smaller contact resistance. The design objective for an ideal TIM hence is low thermal resistance, high compliance and reliability. The excellent mechanical compliance of foams makes it a viable solution for use as a thermal interface material. Additionally, foams, being metallic (high thermal conductivity) have relatively low thermal bulk resistance. The fact that foams can incorporate various gels, thermal greases within their voids and enhance the effective thermal conductivity provides additional motivation for the study.

1.3 Heat Sinks

The primary function of heat sinks is the transfer the heat to the fluid flowing through it so it may be rejected out of the system. It is in essence a heat exchanger transferring heat

to the working fluid. The heat sink is connected to the chip through TIM2-heat spreader-TIM1. The heat transfer mechanism is usually forced convection. The objectives of heat sink design is to maximize the heat transfer and minimize the pumping power required to pump the fluid through the heat sink medium. There exists a trade-off between the pumping work and net heat transferred. Increase in surface area available for heat transfer between fluid and heat sink for enhancing the heat transfer causes an increase in the pressure drop as well. More the pressure drop, more is the pumping work required to pump the fluid through the medium. Another drawback of large pressure drop is that it can cause the working fluid to completely bypass the heat sink and instead flow around the heat sink envelope. Micro channel heat sinks with liquid cooling are one of the viable solutions to meet this requirement. Numerous analytical models have been developed to characterize the performance. Instead of investigating such channel or fin structures, porous metal foams could be a possible solution as heat sinks. The large surface area, 3D dimensional conduction and low effective density provide motivation for studying performance of metal foams as potential heat sinks. Pressure drops for metal foams have been reported to be an order of magnitude higher than conventional heat sinks [15], however even the heat transfer coefficient is relatively higher. It is essential to analyze the trade off with respect to the geometric parameters of the porous materials and evaluate an optimum design in the process in comparison to the conventional finned heat sink.

1.4 Porous Structure

Metal foams or porous structures have been receiving a lot of attention over the years for mechanical applications like energy absorbing, damping, sandwich Low density, large area moment of inertia and relatively high strength make it a more than viable option for the above applications. But recently, the porous structures are being analyzed for use in thermal applications. The large surface area to volume ratio makes them suitable for heat dissipation applications such as heat sinks. Extending the same idea, foams can also be considered for use as Thermal Interface Materials. Metal foams are manufactured by forming bubbles through either inclusion of catalyst in molten metal or creating specific molds. It is usually formed as a Body Cubic Center (BCC) unit cell of the voids. There are multiple ways to approximate or simulate this geometry and are discussed in the subsequent chapter. The existing manufacturing processes can only control the size of the void and total volume fraction of the voids relative to the solid metal. Currently foams comprising of materials such as aluminum and copper are being commercially manufactured.

The porous structure is equivalent to 3D network of metal struts which results it the virtues of large surface area and boundary surface compliance. The metal struts (ribs) on the edge of the surface of the foams can conform to the asperities and voids of the mating surface. This will substantially increase the contact area and consequently enhance the conductance. This material is a step towards engineering custom designs to selectively enhance certain characteristics of the geometry as per the required application. We are

currently limited by the lack of a manufacturing technique to create custom foams, but going forward techniques like electron beam melting and 3D printing are promising and could be used to engineer specific foams in the near future.

For this study we choose porous aluminum structure, but the design is not required to be limited to aluminum or even metal for that matter. The models developed and simulations carried out are flexible enough to encompass any general solid material. All of the analysis is carried out using the 'effective' properties of the porous foams, and these properties are determined the geometry of the structure.

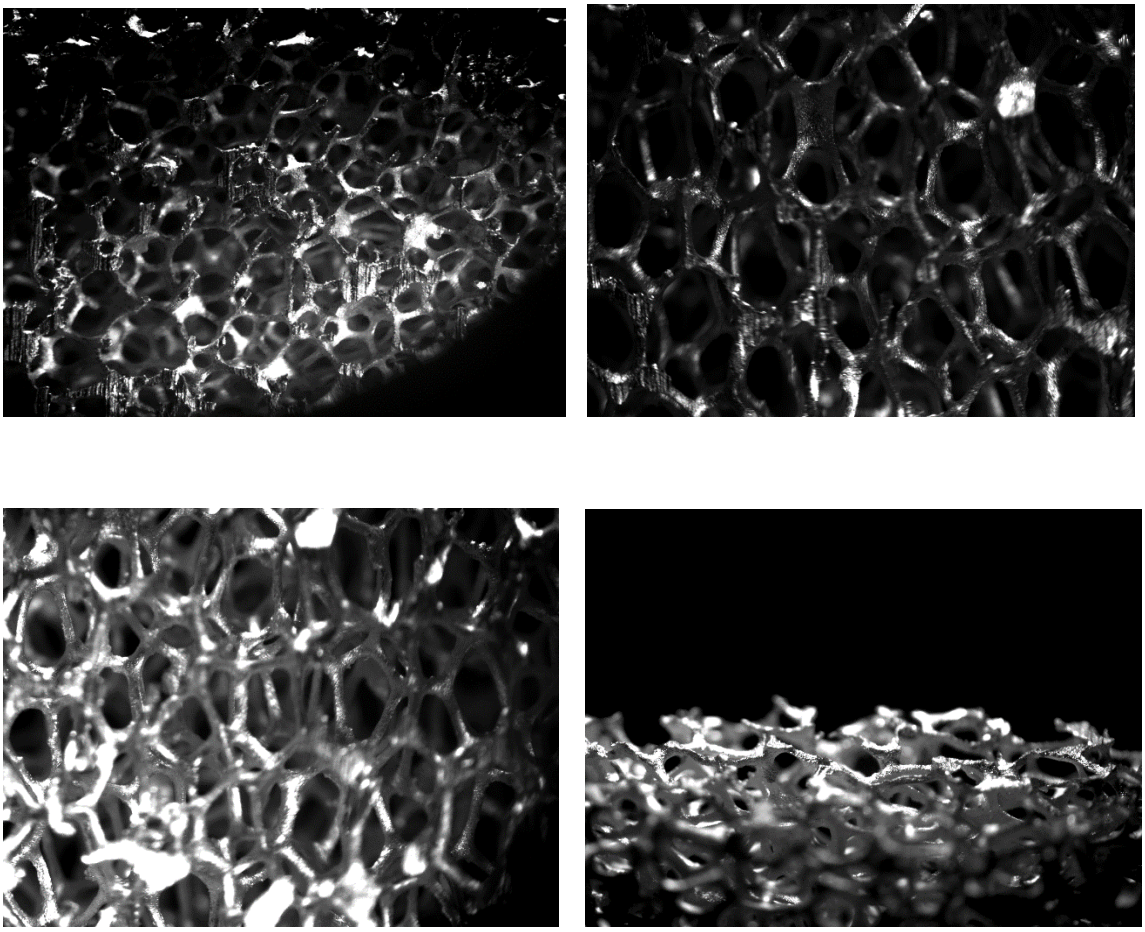

Figure 1.3. Aluminum foam samples.

1.5 Objective

The current needs for enhanced low cost cooling performance could be potentially fulfilled through use of porous structured material. It is predictable that the foams will have lower effective thermal conductivity than the bulk solid, but for the thermal interface design the objective is to have reduced thermal resistance as compared to existing thermal interface materials such as 'stand-alone' gels, greases as well as metal pads. The analysis aims at combining advantages of both, metal pads and thermal greases. Unlike just solid particulate dispersions in grease type thermal interface materials, having metal foam medium in combination to thermal greases in the voids will provide for a continuous path 'highways' for heat flow between the two surfaces in question at the interface, making foams much more suitable for heat conduction

Similarly, for use of foams as heat sinks, before even doing any rigorous calculations it can be mentioned that one would expect the pressure drop across metal foams to be much larger than the conventional finned metal heat sinks, but on the other hand we also expect the heat transfer coefficient and the total surface area available for heat transfer to be significantly larger in comparison. It then comes down to the problem of optimizing this trade-off to come up with the best design. Perhaps the enhanced heat transfer coefficient be worth the additional pumping power required.

This has been the motivation to the relevant properties and performance of porous metal structure in detail in this study. We characterize the mechanical deformation and effective thermal properties in an effort to combine both and develop predictive models

for determining the total thermal resistance and heat transfer performance. We focus on two applications as mentioned above, thermal interface materials and heat sinks.

Simulations are carried for effective thermal conductivity prediction. Additionally, two mathematical models are developed to analytically evaluate the effective thermal conductivity by analyzing unit cell as a representative volume element. Mechanical deformation models are developed based on Timoshenko beam theory and hertz contact theory to predict the area of contact. Experiments are carried out on standard ASME D5470 test setup to find out the total thermal resistance of the material. Multiple permeability and heat transfer coefficient models from literature are evaluated to study the heat transfer for a fluid flowing through the medium for characterization of the performance as a heat sink.

All of the models created and experimentation carried out, is for various different geometric parameters that define the porous structure, like porosity and pore size. This is done so the models are generalized with respect to material and structure. The ultimate goal of the current study is to develop a base to predict the best design for any particular application and going forward even manufacture custom porous structures. The generalized models then, will serve as an effective tool towards better design.

CHAPTER 2. GEOMETRY

2.1 Geometry Definitions

2.1.1 Pore

A pore is defined as one particular 'window' or cavity observed in the structure. It is ideally represented as a circular in shape, but actual foam samples have a hexagon or pentagon pore shape. Depending on the geometry chosen, a unit cell may have one, two or three pores per unit cell. It also depends on how a manufactures chooses to define a pore. In some cases, a pore is defined as an entire spherical bubble, whereas in other definitions the windows or cell walls created by the spherical bubble is called a pore, which can be more than 8 per bubble. Fig. explains this difference.

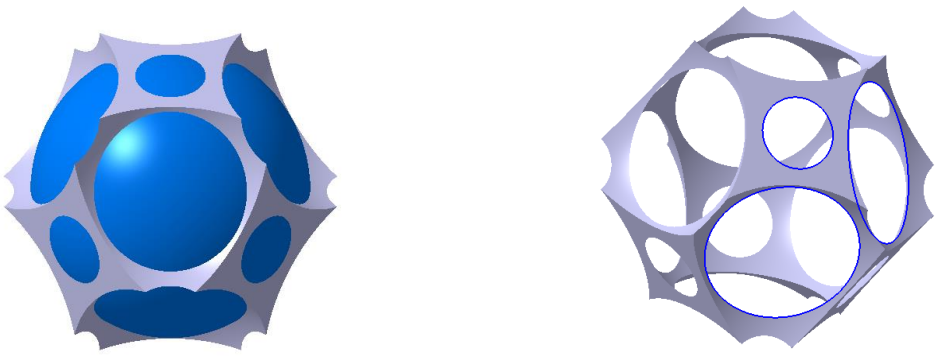

Figure 2.1. Alternative definitions of pore size.

Manufactures usually provide the pore density per inch as specification for the foams. It is then possible to evaluate the pore size from this information if the porosity is known.

2.1.2 Porosity

Porosity is the ratio of void volume in the foam to the total volume of the foam. It is complementary to the relative density. It gives a measure of how much empty volume a foam can have. It is usually between 0 and 1, where 0 represents the solid material. The standard value for the metal foams varies between 0.85 and 0.95. It is an extremely useful parameter to define the foam as most of the effective properties of the foams such as thermal conductivity, young, modulus, permeability etc. can be characterized in terms of the porosity of the foams. The porosity is mathematically defined by:

$$\varepsilon = \frac{V_f}{V_t} = 1 - R. \tag{2}$$

2.1.3 Strut

A strut is defined as the solid ligament which forms a network of the solid phase in the foam. The length of the strut is determined by the pore size and the radius of the strut is determined by the porosity of the foam. Practically struts have a varying cross-section. The shape is referred to as the plateau border, which is actually a triangle with concave sides.

2.2 Representative Volume Element

Most of the analyses available in the literature consider a unit cell or a part of it in order to characterize any specific properties. This basic space filling structure then is specified as a 'representative volume element' (RVE) of the material. The assumption is that the structure is completely homogenous and can be represented by repeating instances of the representative volume element. In such a case, the properties of the unit cell or RVE are the same as the overall properties of the bulk structure [16]. This is a large assumption, but this technique, used in models in the literature give a good prediction of the properties, which are substantiated through experimental data.

Majority of the work in terms of porous structure has been done by analyzing the unit cell or RVE, and the properties then extrapolated to the entire structure. There is an assumption that the medium is homogenous and that the effective properties of the unit cell and the bulk structure will be the same. This is a large assumption, but never the less, authors have shown this to hold true [15]-[20] , through experimentation and computational work. The inherent heterogeneity of the structures does cause variation, but nothing that cannot be predicted within reasonable bounds of uncertainty. Repeatability experiments have been carried out as a part of the experiments done in the study to demonstrate this fact. The challenge then is appropriate selection of unit cell geometry that will most appropriately represent the entire bulk structure.

Different authors use a different approach for selection of 'unit cell' that is analyzed. For the right selection of the representative volume element, it is important to understand

the manufacturing process. Owing to the complicated structure of the foams, most often, the actual geometry of the foams is approximated by simpler geometries which are easier to analyze.

2.3 Manufacturing Process

The typical manufacturing process for foams can be broadly categorized in two possible methods – molten route and powder route. Further classification of the type of foam created depends on the blowing agent used by the manufacturer [21]. The molten route involves melting the metal in presence of a suitable blowing agent such as TiH_2. 'Alporas', 'Duocel', 'Foamcast' are the examples of foams manufactured using this route. There are methods which involve directly injecting gases such as hydrogen while in the molten state to cause foaming of the metal. 'Hydro' foams are one such example. Some metals form a eutectic mixture with hydrogen. Melting these metals in hydrogen atmosphere can result in a homogenous mixture charged with hydrogen ('Gasar' foams).

Powder route involves packing the blowing agent and the metal powder together and subjecting it to heat treatment near the melting temperatures. The homogeneous mixture then decomposes and the gas causes the metal to expand causing foaming. The critical aspect in this process is ensuring a homogeneous distribution of the foaming agent. The details of the process are provided in [22].

A third method for producing foams is having packed salt molds. The molten metals is poured through these molds and solidified. Such methods offer better control over the

structure but unfortunately making the mold is tedious and not commercially viable. However, such methods are useful in manufacturing density graded foams as will be discussed in subsequent chapter.

The properties of the foam can be controlled using a number of factors such as the relative volume of the blowing agent and metal, holding temperature, the foaming time, stabilization methods used etc. [23]. It is possible to control the porosity and pore density using these control factors.

2.4 Geometry Selection

Defining the porous structure geometry mathematically can be extremely rigorous. Dealing with such a model for analytic calculations might not be feasible. It is effective then to consider valid approximations to this geometry such as tetrahedron, honeycomb, tetrakaidecahedron etc. For instance one of the few first analyses used a simple cubic structure in combination with the Lemlich theory, applied to heat conduction [24]. Bhattacharya et al [15] use a honeycomb 2D structure and then integrate the results over multiple layers. Leong et al [19] used a shell cube with spherical pockets at corners to evaluate the thermal conductivity. Various authors have used the tetrakaidecahedron model to analyze the mechanical properties, [25]-[27] as well as the thermal properties,[16][17].

Owing to the nature of the manufacturing process the structure with the minimal surface energy is preferred, and it has been shown the tetrakaidecahedron has been shown to

have minimal surface area out of all the polyhedrons [28]. Hence, foam is considered as repeating units of the space filling Kelvin's Tetrakaidecahedron.

2.4.1 Exact BCC Model

As described earlier, the foam is formed by bubbling the molten metal. The distribution of these bubbles or voids forms a Body Cubic Center (BCC) structured lattice. The bubble and molten metal system tends to a minimum surface potential and results in the formation of the body centered cubic structure. This geometry can be visualized as the subtracting spherical volumes for the bubbles placed at the corner and centers of the unit cell. There are two defining factors to this unit cell. The bubble size and the distance between the bubbles. These factors together determine the porosity and pore size/pore density. A manufacturer usually specifies the foams using the porosity and pore density, which is the easiest to appropriately measure.

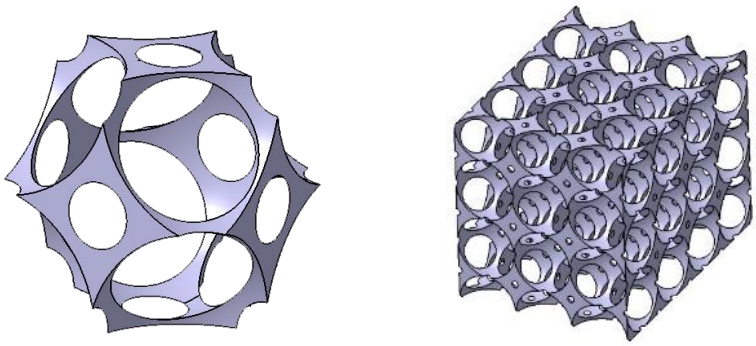

Figure 2.2. BCC model.

This unit cell model is the closest approximation to the actual physical structure. This model can be created in any CAD software and used for simulation purposes. Unfortunately, it is tedious/rigorous to represent this geometry mathematically for analytically characterizing the deformation or thermal conductivity. For this purpose we approximate this model by the following tetrakaidecahedron structure which is relatively easier to represent. The porosity calculations for such a unit cell are given by the following relationship:

$$\varepsilon = \frac{2(\frac{4\pi}{3}r^3 - \frac{\pi}{3}(4r+s)(2r-s)^2 - 2\pi\left(r-\frac{a}{2}\right)^2(2r+\frac{a}{2})}{a^3} \quad (3)$$

where r is the radius of the sphere, *a* is the cube length and *s* is the distance between the void centers.

2.4.2 Tetrakaidecahedron Approximation

The tetrakaidecahedron is the closest approximation to the exact bcc structure. It consists of 8 hexagons and 6 squares. For the actual foam structure all of the mass is contained in the cell ribs and very small or negligible in cell walls. As a result in the tetrakaidecahedron approximation, the sides are considered as cylinders of constant radius. The radius and the length of the sides can be calculated from the known pore density and porosity of the foams. Each of the 14 windows in the symmetrical structure qualify as one pore.

It is convenient to use this approximation for the unit cell for analytic calculations as well as simulations. Recently there has been extensive study on reticulated foams which are based on the tetrakaidecahedron model. Zhu et al [27] have analyzed the effective

mechanical properties using multiple stacked tetrakaidecahedrons. Boomsma et al [16] have analyzed the effective thermal conductivity using similar tetrakaidecahedron model.

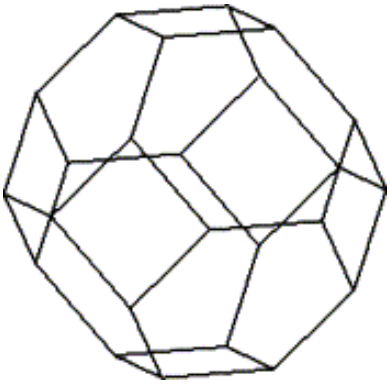

Figure 2.3. Tetrakaidecahedron model.

2.4.3 Tetrahedron Structure

The tetrahedron is a subset of the tetrakaidecahedron model. In cases where even the simplified tetrakaidechedron structure can be complicated for analysis, researches resort to use the tetrahedron structure. Multiple tetrahedron connected in various orientations can be used to represent the tetrakaidecahedron structure. This model is effective for analyzing parameters like permeability and flow fields in metal foams. Duplessis et al [29] have used such geometries to characterize the permeability of foams. The empirical model developed using this structure results in relatively more accurate prediction of permeability of the foams as compared to other models developed using other geometry approximations, such as the honeycomb structure [15] and simple cubic structure [24]. Similarly, such models can also be effective in studying the load transfer mechanism through these struts. This is helpful is evaluating the micro deformations and plastic

collapse of such foams. This geometry has been used to effectively characterize the deformation of the porous structures [30][31].

2.4.4 Hexagonal Structure

The hexagonal honey comb structure is a simplified approximation of the tetrakaidecahedron model itself. It is primarily used for 2 dimensional analysis and simulations. As mentioned before such geometry has been effectively used to evaluate the effective thermal conductivity of the foams [15]. Such structures have also been used to evaluate the effective mechanical properties [32].

The pioneering work in the field of cellular mechanics carried out by Gibson and Ashby [33] was primarily based on the hexagonal geometry. They have developed relationships which effectively predict the mechanical behavior of foams against experimental data.

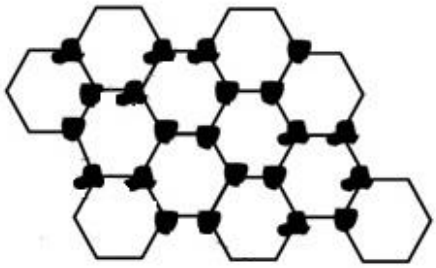

Figure 2.4. Hexagonal structure.

2.4.5 Simple Cubic Structure

The simple cubic structure involves approximating the geometry as orthogonal struts per unit cell, like a cube. It is quite effective, easy to analyze and computationally inexpensive

in case of simulations. This structure is the simplest approximation for three dimensional analysis. Models developed using this approximation to evaluate properties like permeability, effective thermal conductivity provide for considerably accurate results [24]. This kind of approximation is easy to handle in case of simulations as well as analytic models, the downside being this method only gives a first order approximation of the effective properties. A better approximation to the geometry is required when the application demands more precise results.

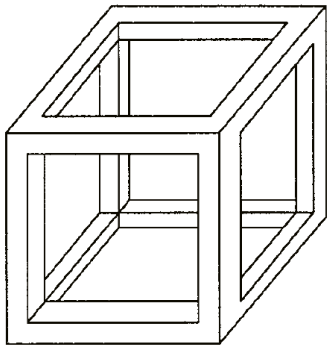

Figure 2.5. Cubic structure.

2.5 Approximations in Present Study

In the current study, the effective properties are analyzed in 3 dimensional space. The exact BCC structure unit cell is used for thermal and mechanical simulations whereas the geometry is modelled as the regular tetrakaidecahedron in case of analytic calculations. To account for the varying cross section and more mass at nodes, the nodes are modelled as spheres. A model has been developed to estimate the relative dimensions of the struts and spheres, based on experimental data in literature.

For the tetrakaidecahedron model, every strut is modelled as a cylinder with radius 'r' and length 'L'. The tetrakaidecahedron has a total of 36 struts out of which 24 are shared with the adjoining unit cells. The side of the cube volume bounding the unit cell is given by$\sqrt{8}L$. Accordingly the porosity expression is:

$$\varepsilon = 1 - \frac{24\pi r^2}{\sqrt{8}^3 \times L^2}. \tag{4}$$

L can be found out using the pore density, which is measured by Pores per Inch (PPI), and then inversely the radius of the strut may be evaluated as:

$$L = \frac{3 \times 0.0254}{\sqrt{8} \times PPI}. \tag{5}$$

If we consider spheres at the nodes, the above equations can be suitably modified to incorporate the mass at the nodes. The expression for porosity is then given by:

$$\varepsilon = 1 - \frac{24\pi r^2 L + 16\pi c r^2}{\left(\sqrt{8}L\right)^3} \tag{6}$$

where c is,

$$c = \frac{R^3}{r^2}. \tag{7}$$

The analytic model extension discussed in the next chapter explains the motive for the specific choice of parameter *c.* All of the above expressions can be derived based on standard geometry considerations and definitions. The variation of the radius of the strut as a function of porosity and pore size is shown in Figure 2.6.

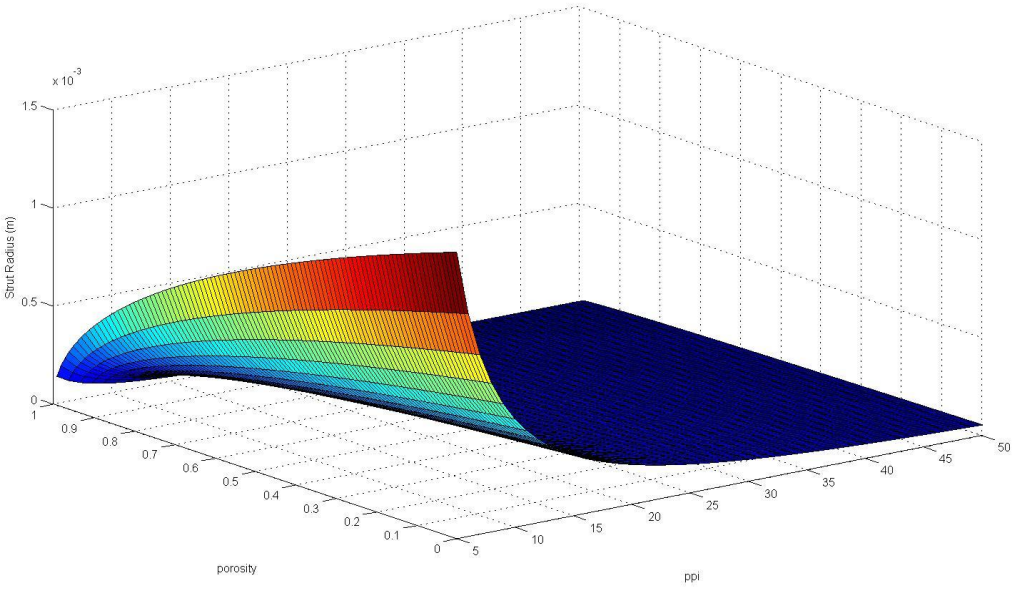

Figure 2.6. Variation of strut radius (Z axis as a function of porosity(X axis) and pore size(Y axis).

CHAPTER 3. BULK PROPERTIES OF POROUS STRUCTURES

3.1 Mechanical Properties

3.1.1 Young's Modulus Analytic Relationship

Metal foams have been a trending research topic in the past with respect to its mechanical properties. The light weight nature and large area moment of inertia make it ideal for use in beams and structures for saving weight without compromising the strength[34]-[36]. These structures are referred to as sandwich structures since they are bound by solid metal plates on either surface. There has been considerable amount of research on determining the effective mechanical properties of porous structure. Most of the recent work is based on the fundamental study done by Gibson and Ashby [33]. They have carried out substantial experimental as well as analytical work and have come up with empirical relationships to determine the Young's Modulus and Yield Stress for foams. In case of elasticity, it has been shown that the effective Young's modulus is directly proportional to the square of relative density:

$$E_{eff} = E_s(1-\varepsilon)^2. \tag{8}$$

Similar results have been reported by various authors on the basis experimental data [25]. A typical stress strain curve for porous structures is represented in Figure 3.1

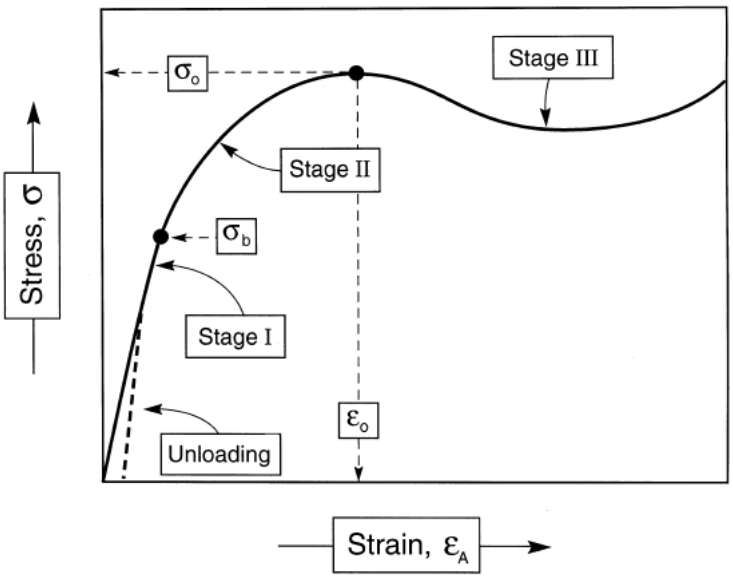

Figure 3.1. Stress-strain curve for aluminum foam.

The empirical relationship has also been verified through numerical studies. Wicklein et al [37] have generated a CAD model from an actual sample of foam and analyzed the mechanical behavior using FEA tools. In other studies, finite element method has been applied to the tetrakaidecahedron model to get the resultant stiffness matrix and subsequently evaluate the effective Young's modulus [25]. Zhu et al [27] have considered the tetrakaidecahedron model and used force/moment balance at specific nodes to analytically derive an expression for effective Young's modulus as a function of the relative density (1-ε). The analytic results are coherent with the experimental data. Work has also been done to extend the same model to incorporate anisotropy [26]. Mechanical properties have also been evaluated in just a 2 dimensional space [32]. The study confirms that the effective young's modulus varies with respect to square of relative density.

A similar kind of relationship can be observed for the yield stress. It has also been observed that the Poisson's ratio doesn't change with respect to the relative density; it remains more or less constant. For a generalized expression-

$$E_{eff} \propto (1-\varepsilon)^{n_E}, \tag{9}$$

$$\sigma_{eff} \propto (1-\varepsilon)^{n_\sigma}. \tag{10}$$

Various authors have reported the following values for n_E and n_σ

Table 2: Comparison of literature models for Young's modulus and yield stress.

Author	n_E	n_σ	Comment
Benouali and Froyen [38]	0.94-2	1.5-2.25	Experimental
Gibson and Ashby [33]	2	1.5	Analytical
Yu and Banhart [39]	1.85	1.7	Experimental
Wicklein et al [37]	1.94	1.94-2.27	Numerical
Zhu et al [27]	2	2	Analytical

The key takeaways from the deformation studies are:

- Effective Young's modulus varies as the square of the relative density of the foams.
- Poisson's ratio is independent of the porosity but depends largely on the geometry
- There is always small amount of plastic deformation on initial loading.
- Foams become stiffer after subsequent loading, unloading and reloading cycles.
- A total plastic collapse occurs in specific bands perpendicular to loading direction

All the above properties make foams virtuous in use as structural members, impact attenuators and vibration absorbers.

3.1.2 Young's Modulus Simulations

Simulations were performed using ANSYS workbench for determining the effective Young's modulus of the porous structure. The results were compared with the analytic models discussed in the previous section. The symmetric unit cell generated from the BCC distribution is considered as the representative volume element for these simulations. The geometry was created using standard CAD software (CATIA V5). The model was applied symmetry condition on all boundary phases. Different boundary conditions were considered – two constant forces acting in opposite directions applied on either ends, constant force applied with fixed displacement on the other end and constant displacement boundary condition. The strain was evaluated from the directional deformation along the direction of application of load. Stress was calculated on the basis of the applied load and apparent boundary area of the geometry. Porosity of the geometry was varied by changing the radius of the voids for a unit constant volume as shown in Figure 3.2. The calculations were based on Eq. 3

Figure 3.2. Variation of porosity (0.83 to 0.99) for simulations.

Dimensionless parameter 'p' was introduced to simplify the porosity calculations. It is the ratio of the void radius to the side length of the unit cell. The table below shows the details of the geometry used for the simulation. Same geometries were used for the effective thermal conductivity simulations in the next section.

The number of elements used in the analysis was varied between 5000 and 15000 depending on the porosity of the geometry. 10-node tetrahedron element SOLID187 was used for the analysis. The results and comparison with the predicted young's modulus from the analytic models is plotted in Figure 3.3

Table 3: Porosities of the geometries used for simulations.

Geometry	p	Porosity
1	0.47	0.838313
2	0.473333	0.850841
3	0.476667	0.863059
4	0.48	0.874963
5	0.483333	0.886546
6	0.486667	0.897802
7	0.49	0.908727
8	0.493333	0.919315
9	0.496667	0.92956
10	0.5	0.939456
11	0.503333	0.948788
12	0.506667	0.957335
13	0.51	0.965088
14	0.513333	0.972034
15	0.516667	0.978162
16	0.52	0.983461
17	0.523333	0.987921
18	0.526667	0.991529

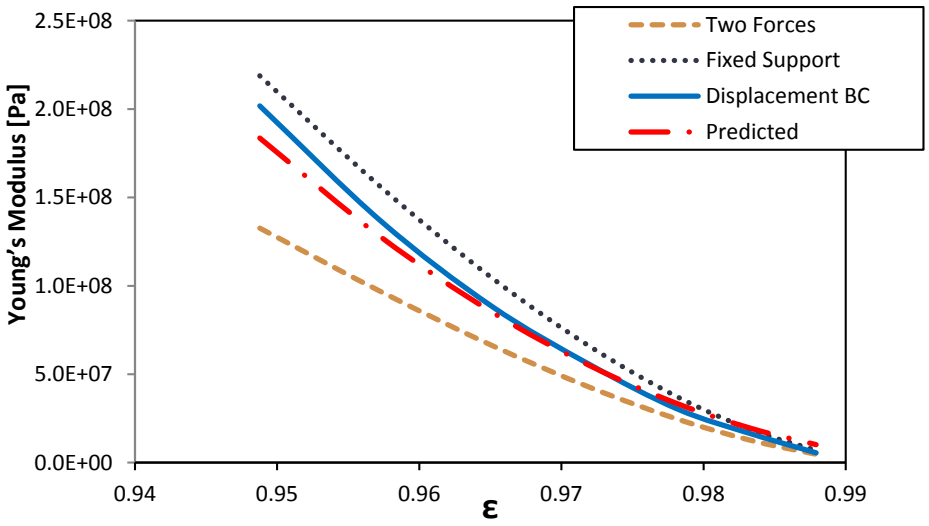

Figure 3.3. Variation of the effective Young's modulus with respect to porosity.

3.2 Micro Deformation

In this study, the mechanical properties of foams are studied, based on the models in literature and the experimental data available. The motive is to develop an analytic model to calculate the actual area of contact in effort to relate it with the contact resistance. The bulk as well as micro deformation is taken into account. As opposed to the macro deformation analyses of the foam which considers the effective properties of the foam, in the case of analyzing the contact area we consider the 'micro deformation' of the foams which is restricted to one or at most two layers of these foams adjoining to the contact surface. The micro deformation model is developed to predict the actual are of contact created by the struts. The deformation is evaluated for a unit cell to determine the actual contact area as a function of porosity. The porosity of the structure affects the radius as well as length of strut for the unit cell. The actual area is then normalized by the apparent area of contact, given by the dimensions of the porous medium in question. The

deformation considerations are restricted to the porous medium side –the opposing contact surface is assumed to be rigid.

3.2.1 Edge Deformation Mechanics

Together, the mechanical properties such as the Young's modulus and geometric parameters such as porosity and pore size, are going to determine the compliance of the porous medium. Actual area of contact can be considered as a measure of the compliance. The contact resistance, as stated before, depends on the area of contact and increases with decreasing contact. As an initial first order approximation for estimating the area of contact, we can consider a homogeneous repeating arrangement of tetrakaidecahedron. The struts of the tetrakaidecahedron are considered to be cylinders of radius '*r*'. The nodes of the tetrakaidecahedron are modelled as spheres. This approximation is made to in an effort to depict the true nature of these porous structures. The diameters of the spheres are determined using the empirical factor 'c' in relation to the strut radius through experimental data. A detail analysis of the estimation of this parameter is provided in the next section. Effective thermal conductivity models developed by various authors [15][16][17] require calibration of a parameter which determines the relative size of the strut and sphere radius. The model, even after incorporating the effect of the calibrated parameter, is valid only over a specific range of porosity. As an alternative to this calibration, it is proposed in this study that the volume aspect ratio of the nodes and struts is constant over all porosities. This eliminates the need of experimental data to calibrate the model. Additionally it has been shown in the subsequent section that such

an approximation actually gives better predictions for the effective thermal conductivity. To maintain the consistency, the same approximation for relative sizes/ volumes of the strut and sphere at nodes are assumed for this deformation study. Using this geometry the deformation is evaluated for a unit cell and then normalized against apparent contact area.

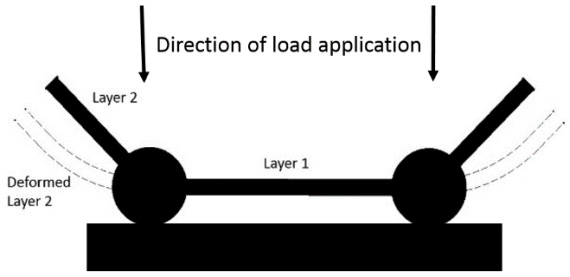

Figure 3.4. Deformation for two layers of tetrakaidecahedron.

For a unit cell, it is hypothesized that the bottommost layer is in contact initially and the 2nd layer struts oriented at an angle of 45°, deform to come in contact with the opposing surface. The individual contribution to area of contact of the two layers adjoining to surface is evaluated. The contact patch for cylinder on flat configuration is going to be rectangular, whereas the contact patch for the spheres at nodes will be circular. For the first layer struts in contact it is assumed that the entire length of the strut is available for contact. The width of contact is evaluated using hertz contact theory. Standard relations from the hertz theory for sphere on flat and cylinder on flat arrangement [40] are applied to get an estimate for the contact area.

In case of second layer contact, the deformation of the strut is evaluated to find out the available length for contact. The Timoshenko beam theory is used to evaluate the contact length of the contact patch. The governing differential equation is given below:

$$E\mathrm{I}\frac{\mathrm{d}^2v}{\mathrm{d}x^2} = M. \tag{11}$$

The above differential equation was solved using an implicit finite difference method to evaluate the deformation. The numerical scheme was implemented using MATLAB. A set of the porosity and the pore-size determines the geometrical parameters of the unit cell. The apparent area of contact is defined as the 'footprint' of the bulk foam structure – a unit cube in this case. The condition for contact of the 2nd layer of struts is that if the angle of deformation at a point is equal to the initial angle of orientation then the contact initiates at this point. In a different context, the point on the strut where the slope of deflection curve is equal to the original angle of orientation of the strut gives us the location where the contact initiates. The length available for contact can thus be found out.

As for the width of contact, it is calculated similar to that for the bottom layer. Only difference in this case is the length available for contact is not the entire length of the strut but is determined from deformed length as calculated from the Timoshenko beam theory. The width of the contact patch is found out using hertz contact theory and for cylinder on flat configuration is given by:

$$w = \left(\frac{4Pr}{\pi E_s l_x}\right)^{1/2}. \tag{12}$$

Observe that the width of contact is also dependent on the length of contact. For the 2nd layer analysis this creates an interdependent relationship. This fact contributes to an already existing trade-off created by the reducing strut size as an effect of increasing porosity. For this particular case we calculate the normalized area of contact for a 50 psi load over a unit area. This is considered as a typical operating load for thermal interface applications in electronics industry. We extend the analysis to study the effect of variation of the orientation of the strut angle as well.

3.2.2 Area of Contact

The two components of area of contact, the width and the length of contact have opposing trends. Figure 3.5 shows the variation of the contact width with respect to porosity for the two layers of the porous medium unit cell. As the porosity increases the width of contact goes on decreasing. This is expected since the radius of the strut decreases with increasing porosity. As for the length of contact, since the radius of the strut is decreasing with increasing porosity, the section modulus decrease as well. This results in more deformation and a larger length of contact as can be observed from Figure 3.6.

The sharp peaks for the width of contact curve correspond to initiation of the contact of the second layer in Figure 3.5. Similarly, when the 2nd layer comes in contact we observe a steady rise in the length of contact Figure 3.6 with respect to increasing porosity. A 3D graph is shown below which gives the variation of normalized area with respect to the

porosity as well as the orientation angle of the 2nd layer struts. Ideally we are interested in the 45^0 angle orientation, but this can serve as a generalized model and can also incorporate any asymmetries/anisotropies within the geometry.

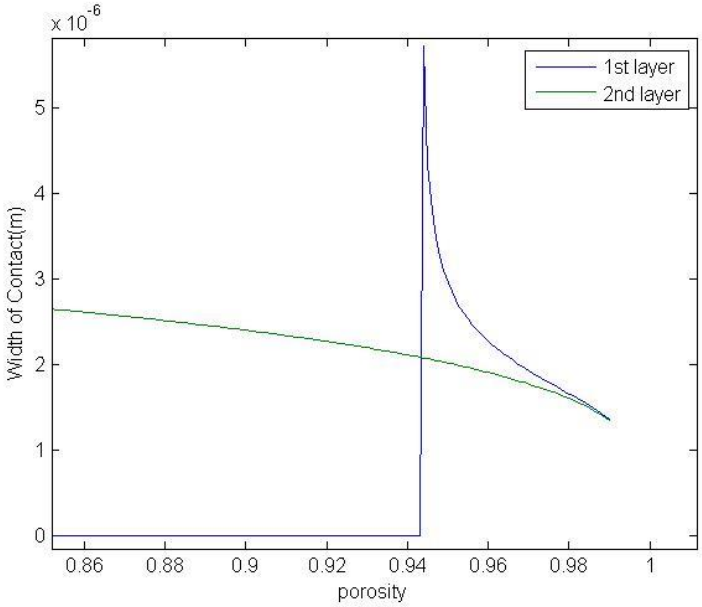

Figure 3.5. Width of contact for two layers.

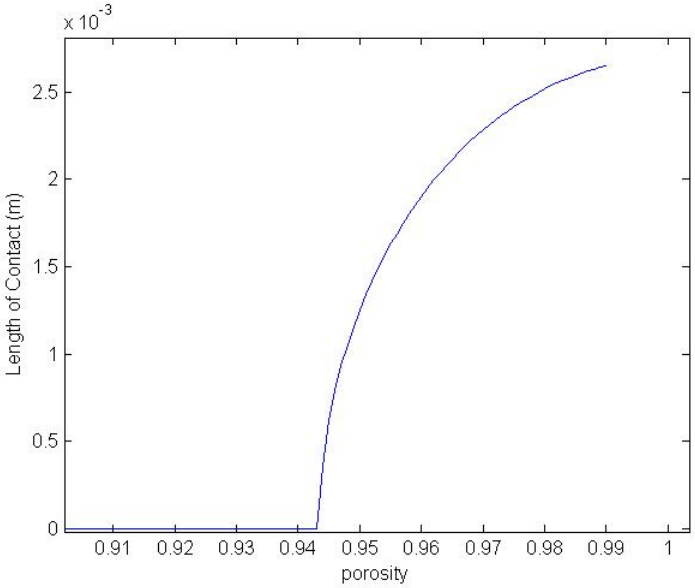

Figure 3.6. Length of contact.

Figure 3.7 shows the variation of the total area of contact. Owing to the competing effects of width of contact and length of contact, we observe a distinct maximum for area of contact. It is observed that the maximum value of area of contact doesn't change with respect to the orientation angle, but the porosity corresponding to the maximum area of contact does change.

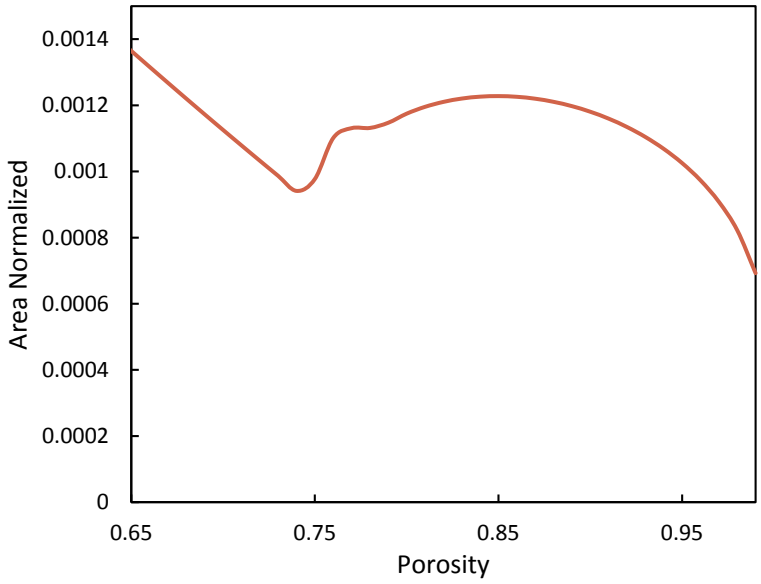

Figure 3.7. Normalized contract area for unit area and 100 PSI load.

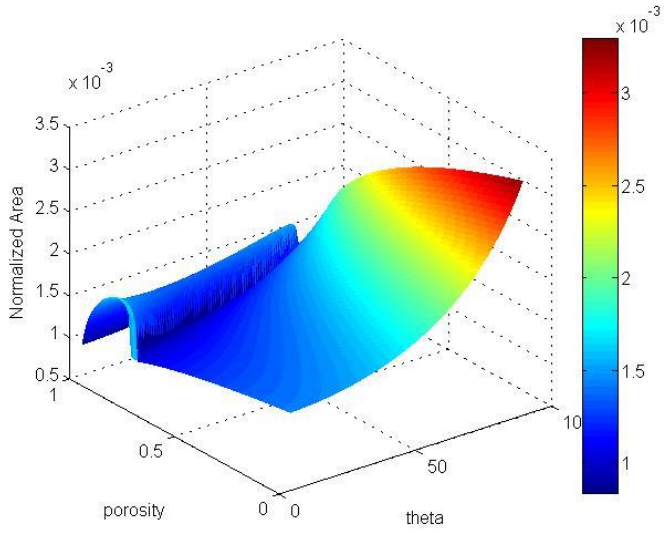

Figure 3.8. Normalized area of contact as a function of porosity and angle of orientation for 100 PSI load 20PPI sample and unit area.

Another interesting result is that, if there is an increase in the total load, the magnitude of the maximum area of contact doesn't change. However, the porosity value corresponding to the maximum area value decreases.

3.3 Thermal Properties

3.3.1 Intrinsic Thermal Conductivity - Analytic Models

The effective thermal conductivity of the foam is expected to decrease with increasing porosity as the effective cross-section area is lesser in comparison. Paek et al [24] have carried out a preliminary analysis for the effective thermal conductivity by considering a simple cubic structure with orthogonal struts. The results give a ballpark prediction of effective thermal conductivity. An extension of this work has been carried out [41], wherein a fraction of total struts are considered to be perpendicular to the direction of

heat flow, and the conductivity is evaluated as a weighted sum of the contribution of the struts in either orientations. Leong et al have developed a rectangular shell model with quarter spherical pockets at the vertices and the model is further sub divided into multiple layers and the conductivity in the layers is evaluated separately. There have been statistical approaches to find out the effective thermal conductivity as well [7] and it has been found that, consideration of radiation effects can further improve the prediction for the effective thermal conductivity.

Boomsma et al [3] have proposed a model wherein a tetrakaidecahedron repeating cell structure is considered and the geometry is approximated by cubes at the nodes and cylinders as the struts for the tetrakaidecahedron. Owing to the symmetry, 1/16th part of the tetrakaidecahedron is considered and the thermal conductivity is evaluated for 4 different sub layers. At each layer it is estimated that the heat conducted in the solid and fluid are proportional to their volume fractions, i.e.

$$k_{eff} = \varepsilon \times k_f + (1 - \varepsilon) \times k_s \, . \tag{13}$$

The same model has been extended [4], wherein certain errors from the previous model have been eliminated and the effect of the orientation of the struts has been incorporated. Bauer et al [42] used a more comprehensive approach to evaluate the effective thermal conductivity, without consideration of a representative volume element. The analysis is based on perturbations in the continuous medium caused by the pores and using energy balance, come up with a governing differential equation. As a result they proposed that the ratio of effective thermal conductivity to the solid thermal conductivity is directly

proportional to the relative density raised to 1/nth power, where the value of *n* is a semi-empirical constant found through experiments. In all of the above literature, the assumption is that the properties of the unit cell will be the properties of the bulk material. Simultaneous conduction in solid and fluid (within the voids) the ratio of heat conducted within each phase is assumed to be proportional to the volume fraction of the respective mediums. The symmetry of the chosen unit cell geometries does not allow the heat flow in lateral directions therefore one dimensional conduction is considered. This assumption has been supported by a thorough experimentation [43]. Additionally, almost all the existing models for effective thermal conductivity do not take into account the inherent heterogeneous nature, density gradients and anisotropy, primarily caused by the nature of the manufacturing process. Additionally, for simultaneous conduction in the fluid as well as solid phase, natural convection and radiation are neglected owing to their minimal contributions to the actual heat transferred.

Druma et al [44] have carried out FEA simulations for heat conduction in array of carbon foam and compared to analytical models [42]. The same author have developed new technique [45] for generating 3D images of carbon structures and subsequently, the same model is used for finite element simulations for heat conduction. There is limited work done on numerical simulations with respect to representative volume element for metal foams.

In this study, simulations are carried out for evaluating the effective thermal conductivity using BCC unit cell model setup. The results are compared with the analytic models from

Boomsma et al [16] and Dai et al [17]. In addition to the extension of the analytic models, an effective resistance model is presented. The calculations are based on first order approximation, and yet this gives considerably accurate predictions for the effective thermal conductivity. The model involves approximating every strut in the tetrakaidecahedron structure as an individual thermal resistance and then consequently simplifying the network to find out one effective resistance in terms of the thermal conductivity of the solid material.

Experimentation carried out for the total thermal resistance using the ASTM D 5470 setup is used to evaluate the effective thermal conductivity as well. The resistance network analogy is compared with results from simulations, the results from the analytic model in the literature, the experimental data from the literature and the experimental data obtained from the experimentation carried out in the current study.

In the existing analytic model extension, resistance network analogy and simulations, the study is restricted to just the solid medium. The void space is assumed to be empty. For including the effect of a fluid in these models, the assumption of one dimensional flow will no longer be valid. In case of resistance network analogy additional resistance networks will need to be incorporated for every point conduction to the fluid. For analytic models, if one dimensional conductions is assumed to be still valid approximation, the conductions through the area not occupied by the solid volume for each layer will have to be considered.

3.3.2 Analytic Model Extension

As discussed earlier the analytic models in the literature have a parameter that needs to be calibrated in order to get a relative approximation for the geometry. As an extension an approximation is develop and implemented in the same model in an effort to evaluate the physical significance of the calibrated parameter. The parameter 'e' used in Boomsma et al is the dimensionless ratio of cube length at node to strut length. The value of this parameter is assumed to be constant over the entire range of porosity. This results in a linear variation of the effective thermal conductivity in relation to the porosity. Instead of assuming this parameter constant, it is assumed that the relative total volume of all the nodes and struts within a unit cell is constant. The parameter is defined as the ratio of cube side raised to the power 3, to the product of square of radius strut:

$$c' = \frac{a^3}{r^2}\,. \tag{14}$$

The volume of the cube varies as cube of side whereas that of the strut varies as square of radius. Since the pore density is considered constant in this analysis, the length of the strut (which also affects the volume of the strut) will be constant for a particular analysis. This constant is then absorbed into the volume aspect ratio constant. Note that for sphere strut arrangement *c* was defined as (R^3/r^2). Physically the volume aspect ratio is adjusted such that the sphere and cube in these two different cases have same volume.

In the formulation created by Boomsma et al, the parameter 'e' (a/L) is replaced in term of strut radius and volume aspect ratio. As a result the final equation giving the relation

between porosity and the geometrical parameters was no longer linear with respect to porosity. The original equation was:

$$\varepsilon = 1 - \frac{\sqrt{2}}{2}\left(de^2 + \frac{1}{2}\pi d^2(1-e) + \left(\frac{1}{2}e - d\right)e^2 + \pi d^2\left(1 - 2e\sqrt{2}\right) + \frac{1}{4}e^3\right). \quad (15)$$

After substituting the parameter '*c*", the final equation becomes:

$$\varepsilon = 1 - \frac{1}{\sqrt{2}}\left(d^2\left(\frac{3\pi}{2} + \frac{3c\prime}{4}\right) + \pi d^{3/8}c^{1/3}\left(\frac{1}{2} + \sqrt{2}\right)\right). \quad (16)$$

The objective is to express the parameters, 'd' and 'e' in terms of porosity and the volume aspect ratio. In this case the values of the d and e are determined in by finding out the root of the above equation numerically using the Newton's method. After the geometric parameters were determined the same expressions for thermal resistances were used to evaluate the effective thermal conductivity.

The issue remains as to what value of *c'* is suitable for the model. The effective thermal conductivity is evaluated over a range of value of *c'* and compared with experimental data. The same analysis is done for the model developed by Dai et al, which is based on the Boomsma model itself. It was found that the variation of thermal conductivity as a function of porosity no longer remains linear. The value of *c'* equal to 0.2 has the best prediction. This value of *c*' physically translates to mean the nodes have 5 times the volume than the struts which seems fair after the total number of struts and nodes and the length of the struts in the unit cell are accounted for.

Between the Dai model and Boomsma model, the latter resulted in a better prediction of the results. The variation of the effective thermal conductivity for different model is summarized in section 3.3.5.

3.3.3 Effective Thermal Conductivity Simulations

In the current study a symmetrical unit cell generated from BCC unit cell is considered as representative volume element for simulating the thermal behavior of the porous structure. Like the literature mentioned above it is assumed that the properties of the structure can be depicted by that of the unit cell. The geometry for the Finite Element Analysis (FEA) model was generated by subtracting spherical volumes from a cube. The dimensions of the cube are equivalent to the size of the unit cell. The centers of the spheres are located at the 8 vertices and the center of the cube. We define a dimensionless parameter p=r/a where 'r' is the radius of the sphere void and 'a' is the cube edge length. The porosity is dependent on the ratio 'p'. Where,

$$p = \frac{r}{a}. \tag{17}$$

Porosity as a function of *p* is evaluated by considering the volumes of the spheres and the intersection of the volumes. The final expression of porosity is given by [46]:

$$\varepsilon = \frac{2(\frac{4\pi}{3}r^3 - \frac{\pi}{3}(4r+s)(2r-s)^2 - 2\pi\left(r-\frac{a}{2}\right)^2(2r+\frac{a}{2})}{a^3}. \tag{18}$$

From the geometry it can be shown that the foam will be open cell if

$$r > \sqrt{(3 \times (\frac{a}{2})^2)} \tag{19}$$

The effect of both, the pore density as well as the pore size is inherent in the ratio '*p*' which will give us expression for the porosity. 18 different geometries were considered, with p varying from 0.466 to 0.533(by varying '*r*', and keeping 'a' constant). These values correspond to the values of 0.825 to 0.996. The high porosity values were intentionally selected to evaluate the lower bound on the effective thermal conductivity.

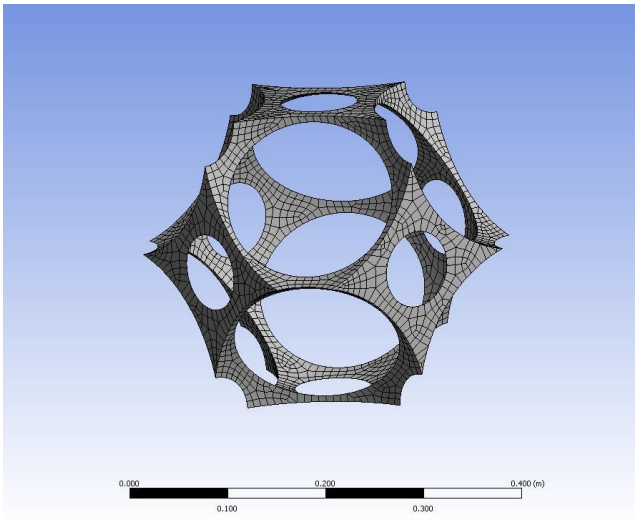

Figure 3.9. Mesh and geometry used for simulation.

3.3.3.1 Boundary Conditions

The model shown in the fig. 7 was used as geometry for the analysis. A constant temperature difference was applied across two opposite faces of the geometry. The thermal conductivity of the solid is assumed to be constant with respect to the temperature. An initial analysis was carried for the geometry at same temperature difference between the two faces but at various absolute temperatures. As expected the thermal conductivity is found to be solely dependent on the temperature difference and not the absolute temperature. Symmetry condition was imposed across the remaining 4 faces of the geometry. Steady state thermal response of the model was carried out using

ANSYS. 18 different geometries with varying *p* (and porosity) were evaluated. Heat transfer by convection and radiation are neglected. Aluminum thermal conductivity value 218 W/mK was applied to the model. This is done so that a comparison could be done with the experimental data available on the aluminum foams as well as the analytic models. A fine mesh was used for the setup. A Hex dominant mesh which had a combination of 'Solid87' (10 node tetrahedral) and 'Solid90' (20 node Hex element) were used for the analysis. The number of nodes varied from 13847 to 90497 and the elements from 4153 to 29068, depending on the geometry in question.

3.3.3.2 Effective Flux and Effective Thermal Conductivity

The heat flux was evaluated at the center section and the total heat flow was calculated by multiplying the flux by the area of the section. Average value of the heat flux was considered as the distribution of the heat flux across the plane is non-uniform. The effective flux was then evaluated for the apparent area of contact. The effective thermal conductivity was calculated for all the geometries using the Fourier's law.

3.3.4 Resistance Network Analogy

A tetrakaidecahedron structure is considered as shown in Figure 3.10. The 36 individual struts of the tetrakaidecahedron are modelled as a resistance given be L/KA_c where, L is the length of one strut, K_s is the thermal conductivity of the solid and A_c is the cross-section area of the strut. Out of the 36 different struts, 24 are shared between the adjoining unit cells. It can be seen that the struts lying in the horizontal planes will not

contribute in the effective resistance owing to symmetry. Using these properties, the final effective resistance can be evaluated as:

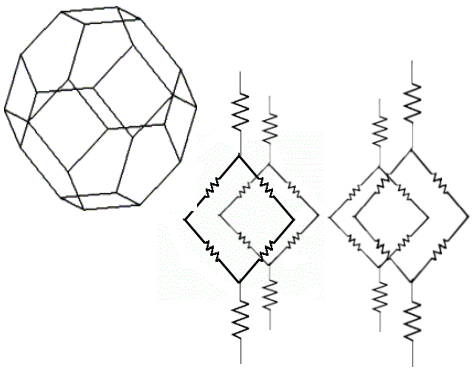

Figure 3.10. Resistance network analogy.

The length and the cross-section area can be evaluated in terms of the porosity and the pore density (pores per inch) usually specified by the manufacturer:

$$1 - \varepsilon = \frac{24\pi r^2 L + 16\pi c r^2}{\left(\sqrt{8}L\right)^3} \tag{20}$$

where c is evaluated as,

$$c = \frac{R^3}{r^2} \tag{21}$$

$$L = \frac{0.0254 \times 3}{PPI\left(\sqrt{8}\right)} \tag{22}$$

and finally,

$$r = \sqrt{\frac{(1-\varepsilon)\left(\sqrt{8}L\right)^3}{\pi(24L+16c)}} \ . \tag{23}$$

These expressions are derived from the definition of porosity, by calculating the solid volume occupied within the bound unit cell. The parameter *c* accounts for the volume occupied by the sphere at the nodes. Every individual resistance is given by:

$$R = \frac{L}{k_s \pi r^2} \ . \tag{24}$$

Substituting these final expressions, we get the effective thermal conductivity as:

$$k_{eff} = \frac{k_s(1-\varepsilon)}{3}. \tag{25}$$

It is interesting to see that the final form of the effective resistance is linearly dependent with respect to porosity, which is similar to the form of other analytic models and simulation results.

3.3.5 Effective Thermal Conductivity Results

The thermal conductivity of the foams was evaluated at porosities more than 0.8 for the analyses so that experimental data as well as analytical results are available in the same range for comparison. The effective thermal conductivities were plotted against porosity, Figure 3.12. In case of simulations, as expected the thermal conductivity decreases as porosity tends to 1.It is interesting however to note, that the trend is almost linear excluding the high porosity range (>0.97). Incidentally all of the other models and data have a linear trend in this particular range.

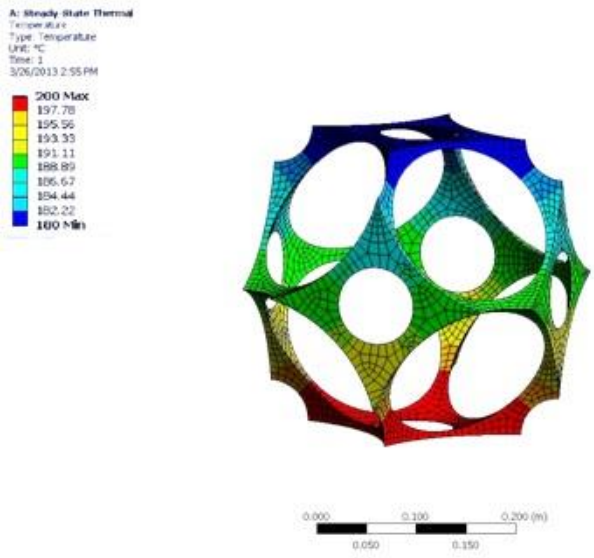

Figure 3.11. Temperature gradient simulation result.

Figure 3.11 shows the temperature variation within the unit cell from the simulations carried out. The assumption of 1D conduction is valid as can be seen from Figure 3.11, wherein the temperature gradient exists only along the Z direction. This was expected and can be attributed to the symmetry of the problem. Additionally, for the heat flux, large concentration was observed near the pores. The average heat flux was then considered for the cross-section selected, in order to compensate for large variations of heat flux on the same plane. The thermal conductivity was calculated using Fourier's law, by evaluating the heat flux for the specific temperature gradient.

The analytical model results and the experimental data from [15] is plotted along with the simulation results in Figure 3.12. The two curves for the analytic model were generated using the same set of equations and input parameters provided in the respective literature As mentioned before the analytical models need a parameter '*e*' to be

calibrated against experimental data. The two curves correspond to *e*=0.198 [17] and *e*=0.339 [16]. The values of the parameters are the same that authors have used for comparison with experimental data in their literature.

It was observed that the analytic models provide for an upper and lower bound to the experimental data. The FEA simulations are shown by the red circular symbols. The simulation results are very close to the values obtained from experimentation. A best fit linear curve is also shown on the same plot. The standard deviation of 0.76 was observed for the experimental data about the best fit curve.

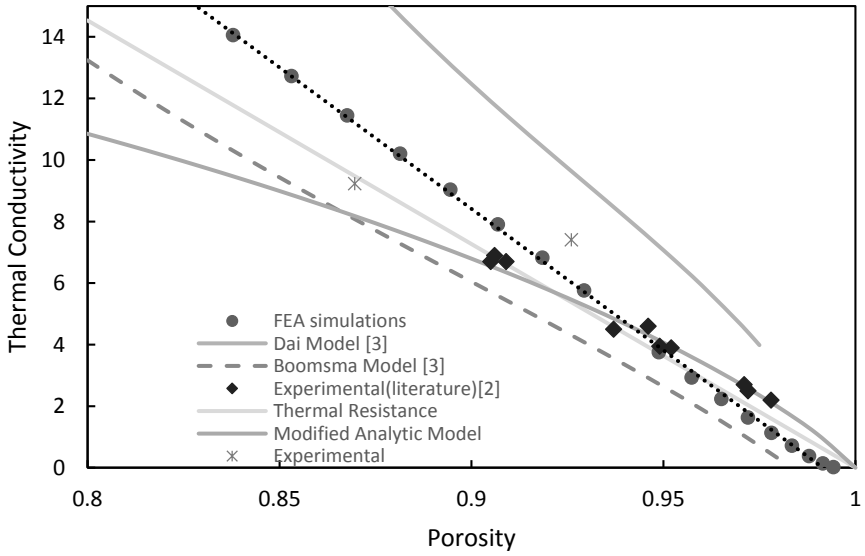

Figure 3.12. Combined results for effective thermal conductivity models.

The resistance network analogy shows a linear trend as well but with a different slope. The prediction with this model is much closer to the experimental data. It needs to be emphasized though that the validity of all of these models is for porosity values greater

than 0.8. It is only in this domain that the geometry approximation of a tetrakaidecahedron is valid.

The extended analytic model can give a good prediction provided the volume aspect ratio is perfectly determined. In this case, the value of the volume aspect ratio was selected such that the model predictions were closest to the experimental results. And as it turns out, such volume aspect ratio lies in the standard range of what is practically observed in foams.

CHAPTER 4. THERMAL INTERFACE MATERIAL

4.1 Experimental Setup- Thermal Contact Conductance Facility

The experimentation is carried out with a test setup complying with ASTM D 5470. The schematic of the test setup is shown in Figure 4.1. The setup consisted two cylindrical 'flux meters' made of electrolytic iron 2.54 cm in diameter and 3.81 cm long. The thermal conductivity of this material is known within 2% (see Appendix A). 4 thermocouples (36 AWG T –type) were embedded within each of the flux meters at the center along the axial direction at a spacing of 0.108 cm. The thermocouples I used in this setup were created by welding 36 T type wire from Omega Engineering. The thermocouples were sealed using an epoxy resin which hardened at room temperature. For calibration the thermocouples were subjected to constant known temperatures using an oven between the temperature ranges of 20 – 80° Celsius at every 10° increment. The controlled temperature and recorded temperature were compared and the curve was linearly adjusted for all 8 thermocouples individually.

A heat source was placed on the top of the flux meter. The heat source was made out of copper and had the same outer dimensions of the flux meter. Three 0.635 cm diameter by 5.08 cm long 100 W Firerod cartridge heaters were placed inside the heat source connected to a Sorenson DCR 20-50B DC power supply. The heat source block was

insulated with one inch thick fiber glass to minimize radiation losses. The heat sink placed at the bottom of the flux meter arrangement had the same design. The heat sink had a 0.635 cm diameter cooling coil wound around it. Ethylene glycol at -10° C was circulated through using Neslab ULT-80 Low Temperature Bath Circulator.

Thermal gap filler HR610 from Laird Technologies was used between the heat source/sink and flux meter to enhance the contact conduction. The column was surrounded by a radiation shield made out of PVC pipe and covered with highly reflective Mylar film coating to reduce radiation losses. These precautions taken are towards ensuring one dimensional heat conduction from top to bottom in the test column.

The column was loaded from below with a 2-way low profile 4-inch diameter pneumatic cylinder. The pressure acting on the column was controlled using a regulation valve on the gas line. The pressure was measured using a load cell mounted on the top of the column above the heat source. The load cell from Omega Engineering, rated up to 1000 lbf, was used to measure the load. It was connected to a DP-25-S Strain Gage Panel Meter for a digital read out.

The sample to be tested was kept between the two flux meters. The experimentation was carried out for 3 different thicknesses – 0.125 inch, 0.25 inch, and 0.5 inch. All three samples were tested for three different porosities of 0.87, 0.93 and 0.95. The samples were manufactured by ERG Aerospace Company and distributed by K.R. Reynolds Company. The porosity of the samples was verified from measurements of the weight and

the external dimensions to calculate envelope volume. Table 4 below gives the details of all the samples used for experimentation.

Table 4: Measured porosity and specifications of samples used in experimentation.

PPI	Rated Relative Density %	Thickness (inch)	Measured Porosity
10ppi	7-9	0.125	0.917956
10ppi	7-9	0.25	0.903817
10ppi	7-9	0.5	0.926007
10ppi	10-12	0.125	0.891154
10ppi	10-12	0.25	0.885423
10ppi	10-12	0.5	0.869561
10ppi	4-6	0.125	0.922547
10ppi	4-6	0.25	0.941125
10ppi	4-6	0.5	0.953314
5ppi	7-9	0.5	0.913288
5ppi	7-9	0.25	0.907782
40ppi	7-9	0.125	0.886707
40ppi	7-9	0.25	0.906425
20ppi	7-9	0.125	0.934206
20ppi	7-9	0.25	0.944856
10ppi	6-8	0.5	0.899349
20ppi	6-8	0.5	0.90217
40ppi	6-8	0.5	0.881967

In addition to this, 0.25 inch, 0.87 porosity, 10 PPI sample was selected for verifying the repeatability of the tests. NetDaq Fluke data acquisition system was used for the temperature data acquisition. A sampling rate of 1 reading/sec was used. The readings were stored and plotted in real time. Additional the trend of temperature change was measured over a period of 300 sec. Steady state was defined as temperatures not varying more than 0.05° C over a thirty minute period. The total thermal resistance was calculated

for steady state. Load on the test column was sequentially increased and resistance calculated at every step.

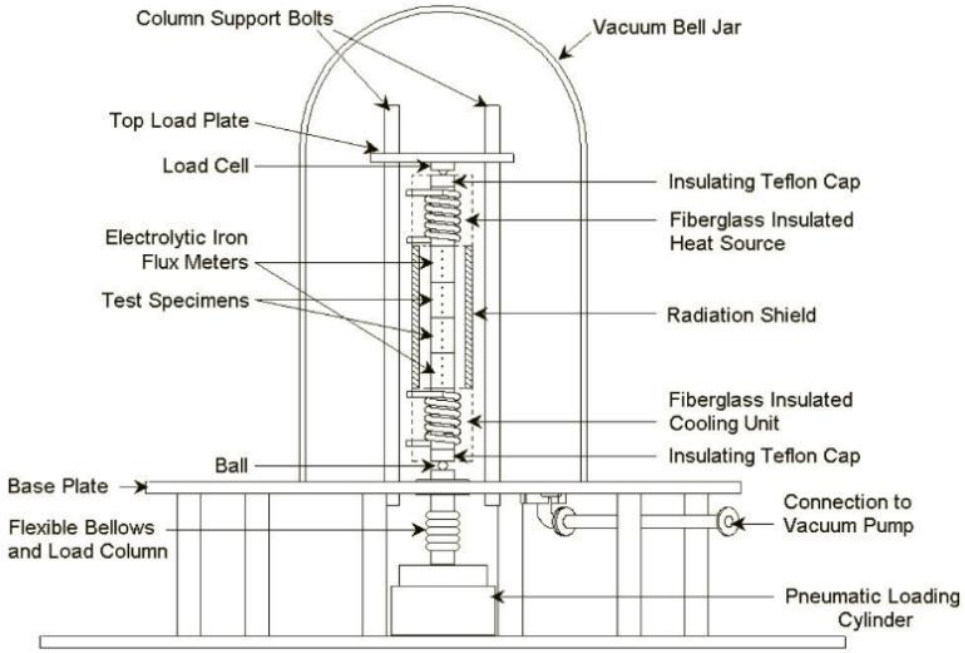

Figure 4.1. Experimental setup schematic.

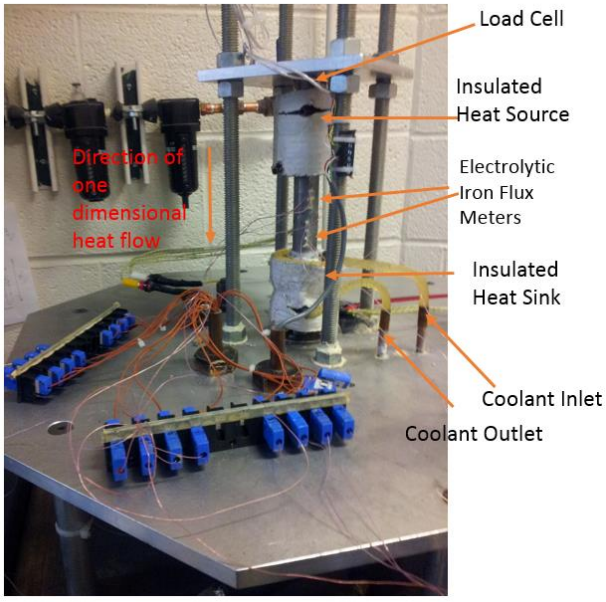

Figure 4.2. Actual experimental setup.

4.2 Total Thermal Resistance Calculation

The heat flux is evaluated from the slope of best linear fit curve for the temperatures of the thermocouple with respect to their locations. The thermal conductivity values as a function of temperature are known within 2% for electrolytic iron (flux meter material). The heat flux is then calculated from the know area, thermal conductivity and the temperature gradient. The net flux across the test sample is taken as average of the two fluxes from the two flux meters. The temperatures at the surfaces of the sample are found out by extrapolating the know temperatures at the 4 thermocouples in each block. Ultimately the resistance is calculated as the ratio of the temperature difference between the two surfaces of the sample to the net heat flux through the sample:

$$Q_{avg} = \frac{Q_1 + Q_2}{2} \tag{26}$$

$$R_{tot} = \frac{T_1 - T_2}{Q_{avg}}. \tag{27}$$

Where T_1 and T_2 are the extrapolated temperatures at the surface of the sample.

4.3 Data Analysis

The temperature data from the data acquisition system was recorded at 1 sample/sec. It was stored in a .csv format. The recorded temperatures were plotted in real time. In addition the slope of the temperature curve over the duration of last 300 sec was plotted. In accordance to the steady state definition, slope between $\pm$ 0.00027 signified the system had reached steady state. After initiating the apparatus, it took about ~5000 sec for the system to reach a steady state. The load was incremented after recording the readings at

steady state for 300 sec. It took ~40 minutes for every subsequent steady state after load increment. The Figure 4.3 below shows the raw temperature data against time axis. The surface temperature are extrapolated and flux evaluated from this data.

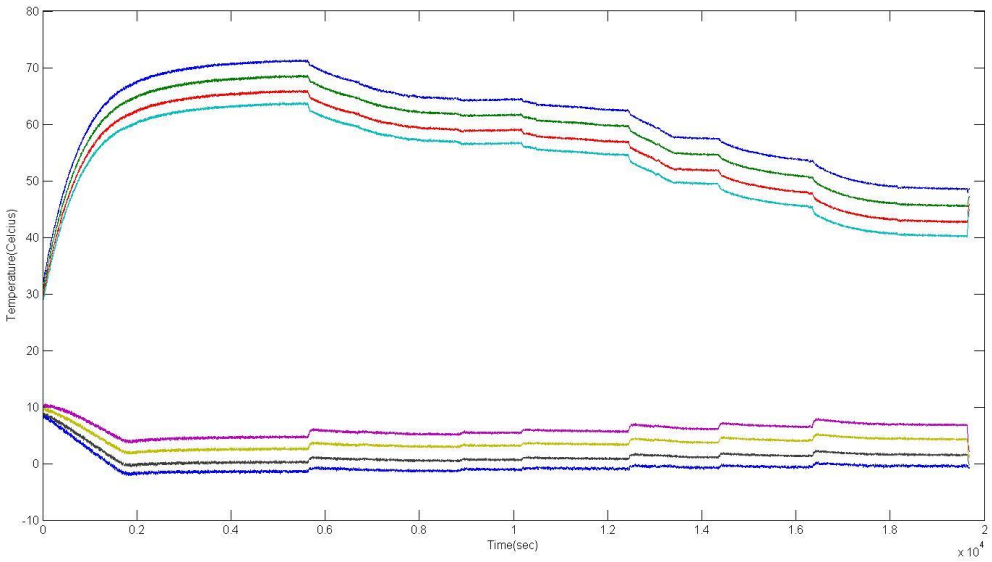

Figure 4.3. Raw temperature v/s time data for 40 PPI sample 0.9 porosity.

4.4 Uncertainty Analysis

The total effective uncertainty of the overall thermal resistance is calculated based on the uncertainty of the individual measurements of temperatures, dimensions of the parts and material properties. The uncertainty analysis was performed as per the method outline in [1]. The generic formula to find an uncertainty is given by:

$$r = r(X_1, X_2, \cdots X_J) \tag{28}$$

$$\frac{U_r^2}{r^2} = \left(\frac{X_1}{r}\frac{\partial \mathrm{r}}{\partial \mathrm{X}_1}\right)^2 \left(\frac{U_{X_1}}{X_1}\right)^2 + \left(\frac{X_2}{r}\frac{\partial \mathrm{r}}{\partial \mathrm{X}_2}\right)^2 \left(\frac{U_{X_2}}{X_2}\right)^2 + \cdots + \left(\frac{X_J}{r}\frac{\partial \mathrm{r}}{\partial \mathrm{X}_J}\right)^2 \left(\frac{U_{X_J}}{X_J}\right)^2. \tag{29}$$

The same formula is applied to the functions used to extrapolate temperatures, calculate flux and eventually overall thermal resistance:

$$R_{contact} = \frac{T_d - T_e}{Q_{avg}} \tag{30}$$

$$U_{R_{contact}} = \left[\left(\frac{U_{T_d}^2}{(T_d - T_e)^2} + \frac{U_{T_e}^2}{(T_d - T_e)^2} + \frac{U_{Q_{avg}}^2}{Q_{avg}^2}\right) * R_{contact}^2\right]^{1/2} \tag{31}$$

$$Q_{avg} = \frac{Q_1 + Q_2}{2} \tag{32}$$

$$U_{Q_{avg}} = \left[\frac{U_{Q_1}^2 + U_{Q_2}^2}{4}\right]^{1/2} \tag{33}$$

$$Q_i = -A_i k_i \frac{T_m - T_n}{x_m - x_n} \tag{34}$$

$$U_{Q_i} = \left[\left(\left(\frac{U_{A_i}}{A_i}\right)^2 + \left(\frac{U_{k_i}}{k_i}\right)^2 + \left(\frac{U_{T_m}}{T_m - T_n}\right)^2 + \left(\frac{U_{T_n}}{T_m - T_n}\right)^2 + \left(\frac{U_{x_m}}{x_m - x_n}\right)^2 + \left(\frac{U_{x_n}}{x_m - x_n}\right)^2\right) Q_i^2\right]^{1/2} . \tag{35}$$

The individual uncertainties for the basic measurements are listed in table below:

Table 5: Uncertainties of the experimental setup.

Variable	Temperature	Column Diameter	Axial Thermocouple Location	Electrolytic Iron Thermal Conductivity	Column Axial Load
Uncertainty	0.2 K	0.00254 cm	0.0127 cm	2%	0.1 lbf

4.5 Sensitivity Analysis

A sensitivity analysis was performed in order to evaluate the relative importance of the inherent heterogeneities in the structure and its effect on the overall thermal resistance. A screening method proposed by Cotter was used for the analysis. The advantage of using such a method is to require relatively fewer data points for analyzing the relative impact of individual parameters. This method occasionally fails to identify key parameter and it

cannot quantify the contribution of individual parameter. It is a first order approximation of the relative importance of the parameters.

If *n* parameters are considered for the analysis, 2*n*+2 simulations/cases would be required to evaluate the relative importance. The 'high' and 'low' is defined for each parameter depending on the uncertainty. The zero case is considered with all chosen input parameters at low value, whereas the final case is with all parameters in 'high' value. The case 1 to *n* are carried out based on case zero with one parameter set to high sequentially. The cases *n*+1 to 2*n* are based on final case with each parameter set to low value sequentially. The relative importance of the jth parameter is calculated by the following relationship:

$$M(j) = \left|y_{2n+1} - y_{n-j} + y_j - y_0\right| + \left|y_{2n+1} - y_{n+j} - y_j - y_0\right| . \quad (36)$$

Where *y* is the output of interest, area of contact in this case. For this study, the controlling parameters that could create heterogeneity are considered. 4 main parameters are chosen - Pore density (PPI), porosity, angle of struts and the Young's Modulus. The high and low values for each parameter as well as the relative importance evaluated are listed in the following table.

Table 6: Relative variations and sensitivities of controlling parameters.

j	Parameter	High	Low	Rank(highest sensitivity)
1	Porosity	0.94	0.86	2
2	PPI	30	20	1
3	Theta	55	35	4
4	Young's Modulus	7.53E+10	6.67E+10	3

The porosity variation is 4% and pore density is 10PPI as per the manufacturer specifications. The strut angle variation is assumed to be 10° and the Young's modulus uncertainty of 6%.

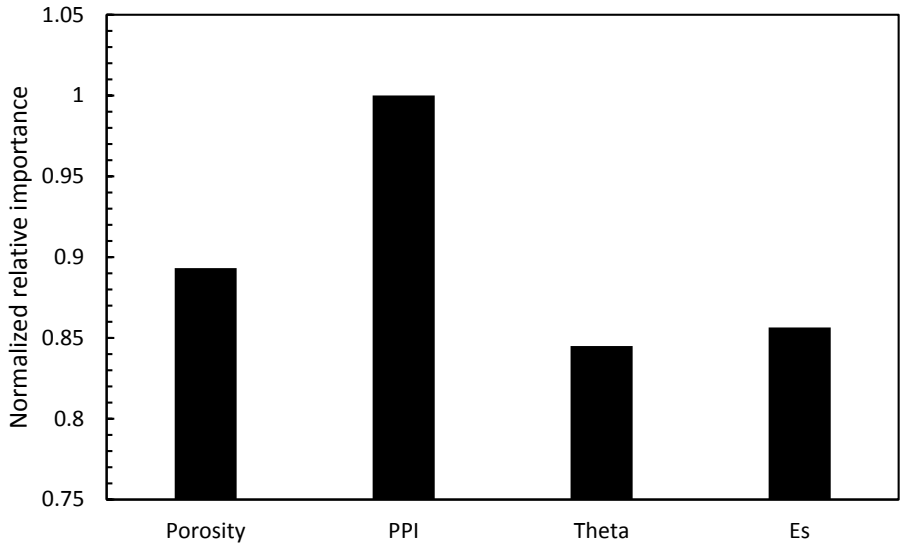

Figure 4.4. Relative importance of parameters for area of contact.

According to the computed results, it is evident that the final area of contact model has a maximum sensitivity to the pore density. This means even a small variation in the pores per inch can cause a large variation in the actual area of contact. Porosity is the second most sensitive parameter.

4.6 In Situ Thickness Measurement

An unconventional method for in situ thickness measurement was implemented in the experiments performed. Two horizontal marks were created on the flux meters all along the periphery. During operation and loading the assembly was perpendicularly

photographed from a fixed point using an 8 MP camera with a resolution of 3264x2448. The exact size of the flux meter was known. Pixels between the two marks and also that occupied by the flux meter were measured. Since the measurements were always relative to the flux meters size, the distance between the two marks can be found out for every loading. The difference between every successive loading was evaluated and the deformation found out. Matlab code was used to measure the pixels in the perpendicular distance between the two marks and flux meters. Figure 4.5 shows a sample reading

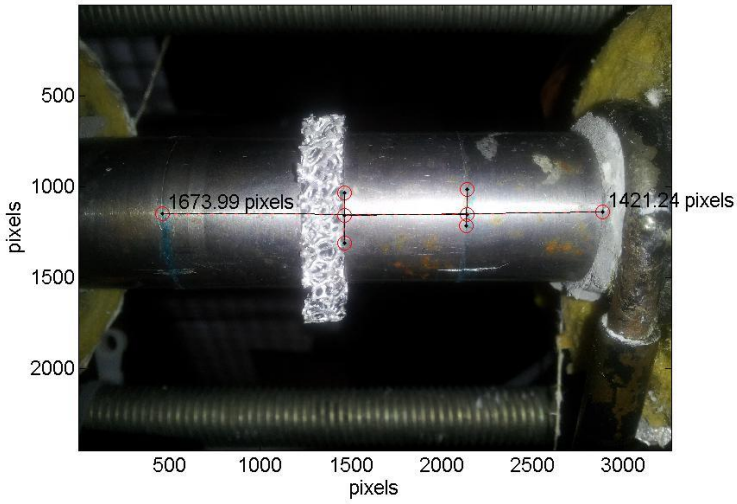

Figure 4.5. Thickness measured using pixels.

4.7 Results

The experimental values for the total thermal resistances through Figure 4.6. The results are plotted for the three thicknesses for specific porosity of 0.87 in Figure 4.6 (a), 0.93 in Figure 4.6 (b) and 0.95 in Figure 4.6 (c). As expected the thermal resistance drops drastically with every increment in load for smaller loads and tends to a constant value for larger loads. For smaller porosity values (0.87 and 0.93) the resistance is larger for

larger thickness in both the cases. The 0.125 inch sample shows almost a linear trend. Whereas the 0.25 inch and 0.5 inch sample are seen to asymptotically converge to a specific value. This is not the case for large porosity samples as seen in Figure 4.6 (c). The 0.5 inch thickness sample has a smaller resistance than the 0.25 inch and 0.125 inch thickness sample for higher loads. If comparison is done only for a specific thickness (0.5 in) in this case, across different loads for multiple porosities, we observe that for the higher porosity (0.95) the thermal resistance actually has a smallest of the three thermal resistance value.

From any two curves from this set, the contact resistance and thermal conductivity can be evaluated for a specific porosity. There are three equations possible from choice of any two curves to evaluate two unknowns of bulk and contact resistance. The equations are solved simultaneously to find the 'best fit' solution. The effective thermal conductivity is plotted in Figure 3.12. The contact resistance is dependent on both, porosity as well as the applied load. As expected the contact resistance decreases monotonically as the load increases.

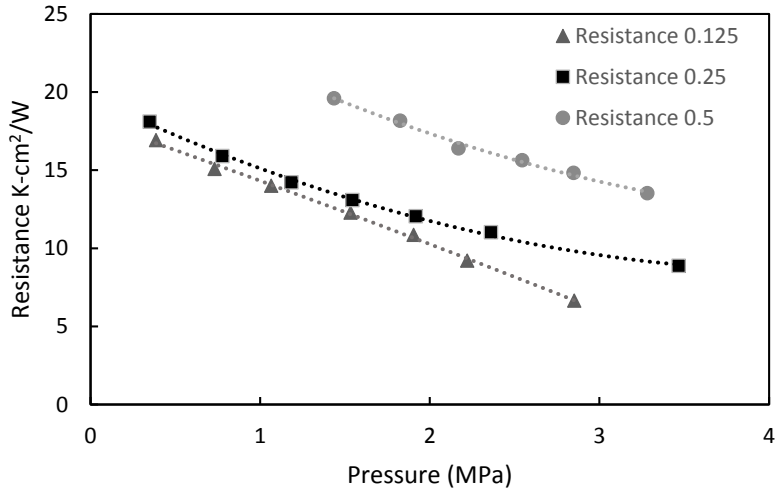

(a)

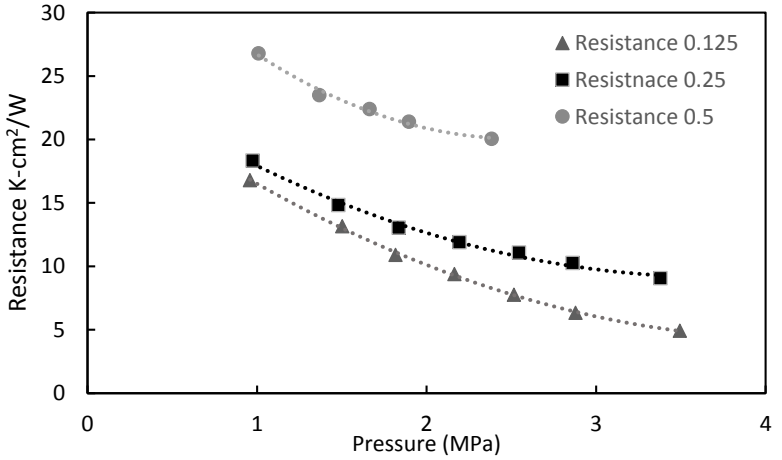

(b)

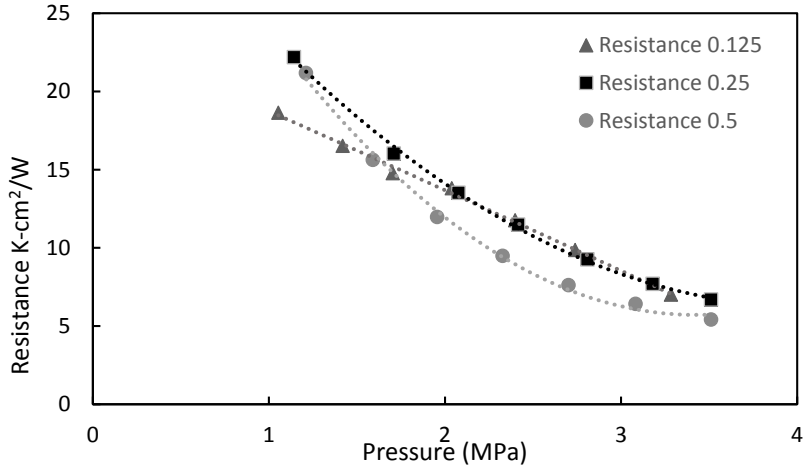

(c)

Figure 4.6. Resistance of various porosity (a)10-12% (b)7-9% (c)4-6% samples as an effect of pressure.

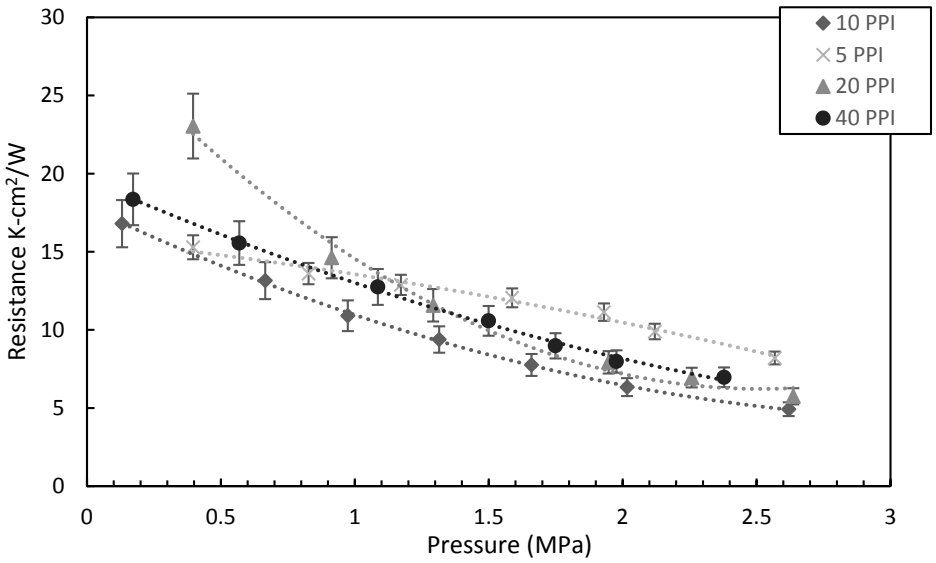

Figure 4.7. Variation of PPI.

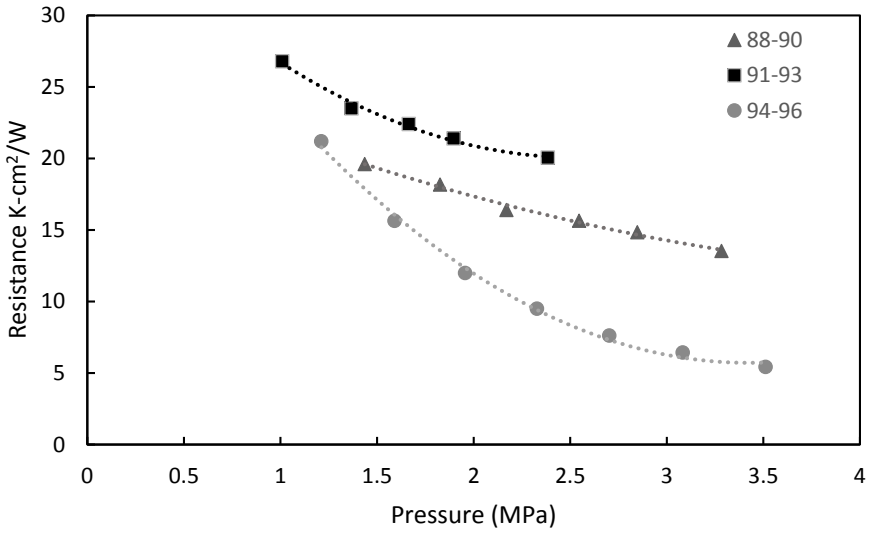

Figure 4.8. 0.5 inch sample with various porosities.

It is observed from the area of contact curve Figure 3.7 that there exists an optimum porosity corresponding to maximum area of contact. If we plot the total thermal resistance values against the porosity, we observe the high porosity samples show a drop

in the thermal resistance curve. This effect is more prominent at higher loads. The thermal resistance beyond the optimum point is naturally going to tend to infinity (or extremely large) as the porosity increase up to 1. In this experimental data, there also exists an optimum porosity corresponding to minimum thermal resistance.

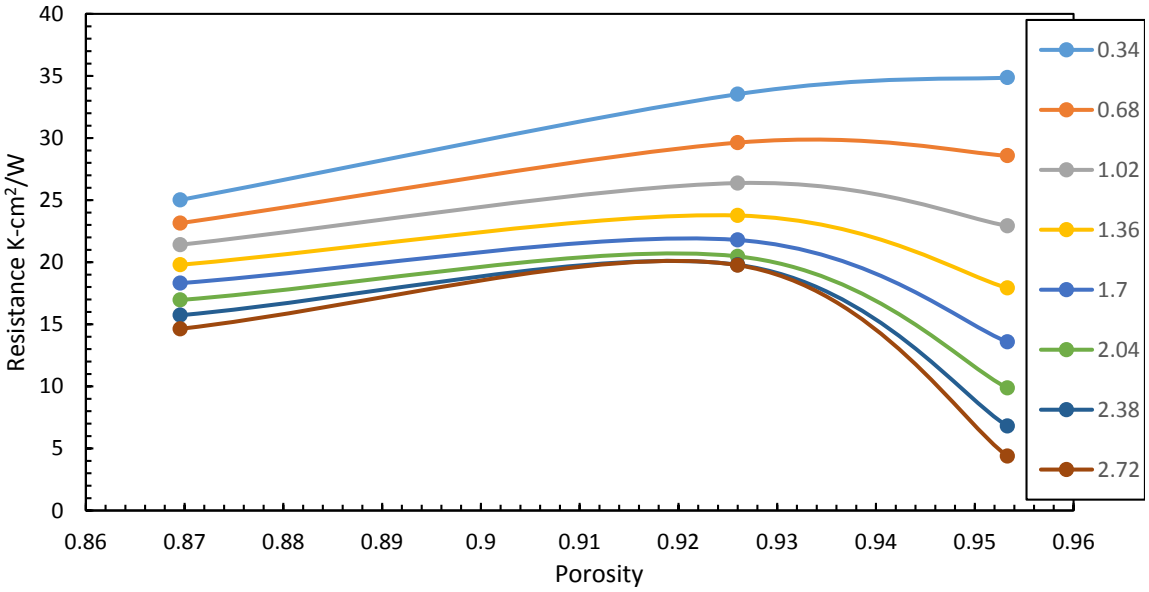

Figure 4.9. Total thermal resistance against porosity for multiple load cases.

The experimentally observed trends hint towards to competing effects that determine the total thermal resistance (Figure 4.9). As porosity increases the effective thermal conductivity is going to reduce and hence the bulk thermal resistance is going to increase. But since we observe a drop in the total thermal resistance, it can be inferred that contact resistance is decreasing. This implies there might be a substantial increase in the contact area. This observation is coherent with the contact area analytic model developed. These two effects are analogous to the length and width of the contact patch observed in the analytic models developed for the area of contact. As the length of deformation will go

on increasing the contact area will go on increasing and consequently the resistance will go on decreasing. Beyond a point the decreasing width of contact becomes a dominant factor and hence as the porosity increases, the area of contact will reduce and the thermal resistance will start increasing.

For the higher porosity data, it can be seen that the thermal resistance curves for multiple thicknesses merge together and the largest thickness sample actually shows the minimum thermal resistance. One possible explanation to this observation could be that the effective Young's modulus is relatively very small for high porosity values. As a result there is excessive deformation which possibly leads to better compliance of the porous medium against the opposing surface. Larger the thickness more is the compliance of the sample. This implies that the contact resistance is a function of the thickness of the sample. This needs to be investigated in further detail.

4.8 Repeatability

A large assumption of the study has been that the sample heterogeneity is small and it is feasible to consider it almost homogenous. This could be justified as the micro heterogeneities can in fact get 'averaged' out owing to the large number of unit cell and struts. This assumption can be verified from experiments if multiple sample with the same specifications is subjected to similar operating conditions. In the study, 0.25 inch samples with 10 PPI and 0.88 porosity were tested for repeatability. In all cases the samples were

subjected to same boundary conditions. The figure below shows a comparison of the thermal resistance of the samples tested.

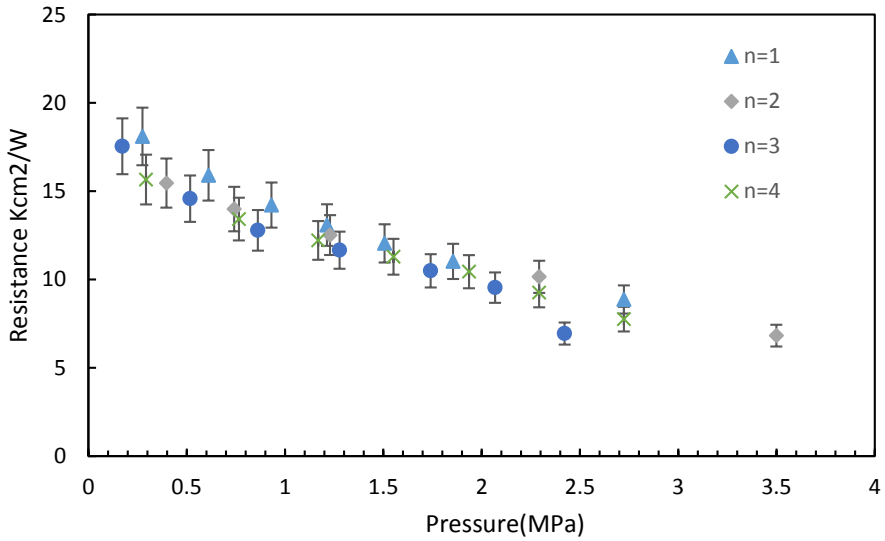

Figure 4.10. Repeatability data, 10PPI 0.88 porosity.

4.9 Thickness Measurement

The thickness measurement results are plotted in Figure 4.11. The results are not very useful as the deformation is negligible for the loads used in current study. Only the final load case which is stresses the sample beyond the yield stress of the material shows significant deformation. The resolution obtained was 20 microns with the current measurement technique.

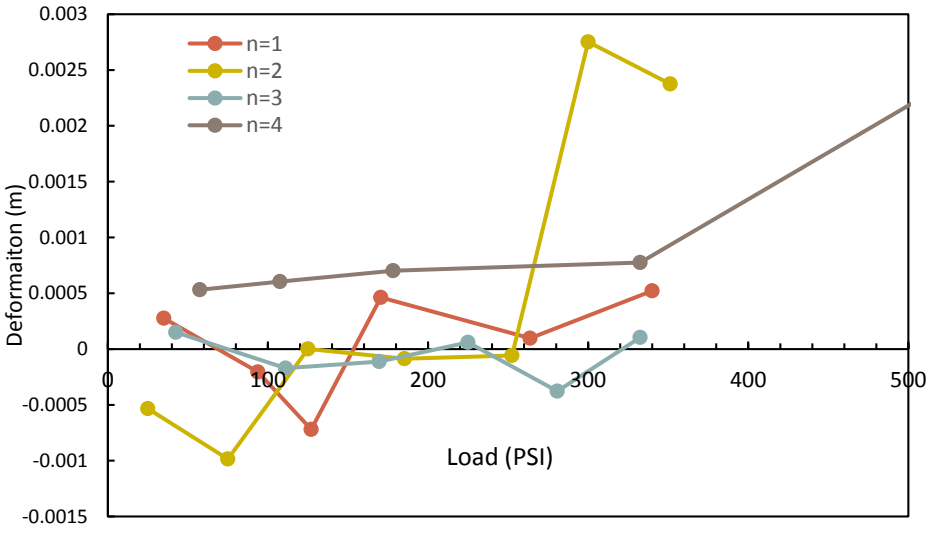

Figure 4.11. Thickness measurement results for 0.25 inch 10 PPI 0.88 porosity samples.

CHAPTER 5. HEAT SINK

5.1 Introduction

A porous structure is evaluated as a potential option for heat sinks. A generalized analytic model is developed to characterize the heat transfer and pumping work (pressure drop across the heat sink). In order to achieve a cost specific or energy specific maximum performance of the heat sink, there is a need to analyze the dependency of the design parameters, i.e. hydraulic diameter, channel length, etc. an optimum design is found out by evaluating the trade-offs in the impact of design parameters. For simplicity and generalization of the heat sink geometries, this work considers a porous heat sink as a representation of general heat sinks. The performance and pumping power is characterized as an effect of porosity and pore size. This study presents an analysis on the cooling performance of aluminum foams used as heat sinks, by considering the interdependence of the different factors such as effective heat transfer coefficient, pressure drop, and permeability. These parameters are functions of design variables - porosity, pore density and the dimensions of the heat sink. The relationship between these parameters and porosity/pore size are studied. The porosity and pore size, in turn are inter-dependent as well, which results in a complicated coupled relationships for the heat transfer rates as well as pumping work.

This work further provides a generic model to encompass the dependence of pore size and porosity. For the sake of comparison with conventional heat sinks, the coefficient-of-performance (COP) of the porous heat sink is evaluated. COP represents the ratio of the heat rejected to the power supplied. The impact of the material properties, such as density and thermal conductivities of the solid /fluid, including the viscosity of the fluid are also investigated. We introduce a figure-of-merit (FOM) defined to give a quantifiable measure of the cost to performance ratio. . The mass of the solid material is assumed to be linearly dependent to the heat sink cost, which is reasonable assumption for a large scale manufacturing based on an industrial experience of one of the author. COP and FOM provide a performance measure and help in selecting the best design. The goal is to maximize the FOM and the COP.

It is expected that both, the pumping power required and the net heat transferred, decrease with increasing porosity and/or pore size. The objective is to maximize the heat transfer and reduce the pressure drop at the same time. Here lies the trade-off which is evaluated using COP and FOM. An extended study on density (porosity) and pore size graded (linear and quadratic) foams along the x-direction (see Figure 5.1) is presented.

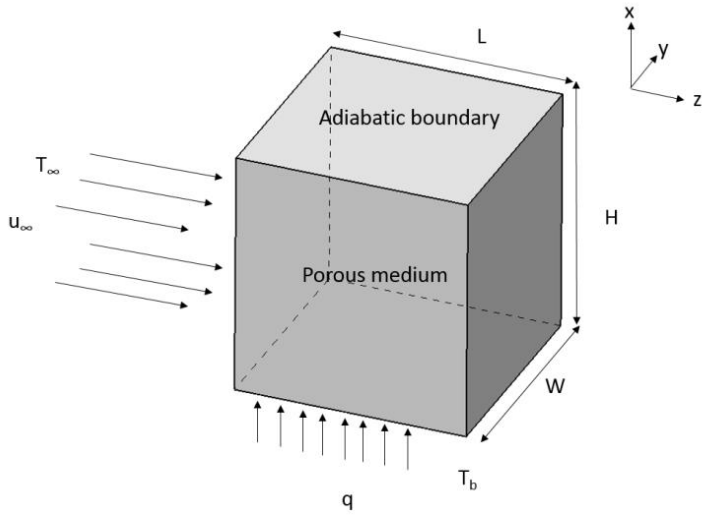

Figure 5.1. Heat sink schematic.

5.2 Model

The model used in the study is a 'one-equation' model. A one dimensional heat conduction is assumed, and the heat sink is analyzed as a fin, by considering effective properties of the porous medium. The model considers a constant heat flux condition at the base of the heat sink. The other end is adiabatic. Fluid (in this case air) flows through the medium, perpendicular to the direction of the flow as represented in the schematic Figure 5.1.

This 'one equation' model translates to mean existence of local thermal equilibrium at the pores between solid and fluid phases so that the temperature field can be evaluated using a single governing differential equation. This kind of model might not be suitable if water is the working fluid. A large difference in the local temperature is observed between the solid and fluid phases when water is the working fluid. This makes the initial

approximation of local thermal equilibrium invalid. However in case of air as the working fluid this model has been shown to be effective [43] and additionally simplifies the already complex analysis for the porous medium. Analyzing the flow field through the porous structure is analytically not feasible. A qualitative understanding of the flow involves formation and disintegration of a boundary layer along the pores. Coupled with constantly changing cross section area in flow direction and due to the inherent heterogeneity in the porous structure, it is difficult to achieve an exact analytic solution. Hence, numerical solutions or the correlation based models have dealt with 'volume averaging methods' [47]

5.2.1 Permeability

The permeability is a measure of the ability to allow flow of the fluid though the medium. It is a function of porosity, pore density, interconnectivity, orientation of the struts, and tortuosity [48]. The analyses in literature discuss porosity as the primary variable which affects the permeability. Experimentally it is determined using homogenized version of Darcy's law [49]-[54]. The experimental data for a variety of porous material including metal as well as organic foams [48], [52]-[54] suggests that the permeability is an exponential function of the porosity. With more careful consideration, however, this exponential relationship holds true only for high porosity (> 0.7) values and the permeability varies linearly with the porosity at low values of porosity (<0.7) [52]. Additionally, experimental data [11] suggests that the dependence on the porosity decreases as the pore density increases.

5.2.1.1 Correlation Model

As an initial analysis, a constant pore size model was developed. As simple correlation was established between the porosity number and the permeability from the available experimental data [15]. A co-relation of the form:

$$K = ae^{b\varepsilon} . \quad (37)$$

was established and the coefficients 'a' and 'b' determined from experimental data . The downside for this model was that it doesn't incorporate the effect of variation of pore size. As a result the initial analysis had to be done for a constant pore size model.

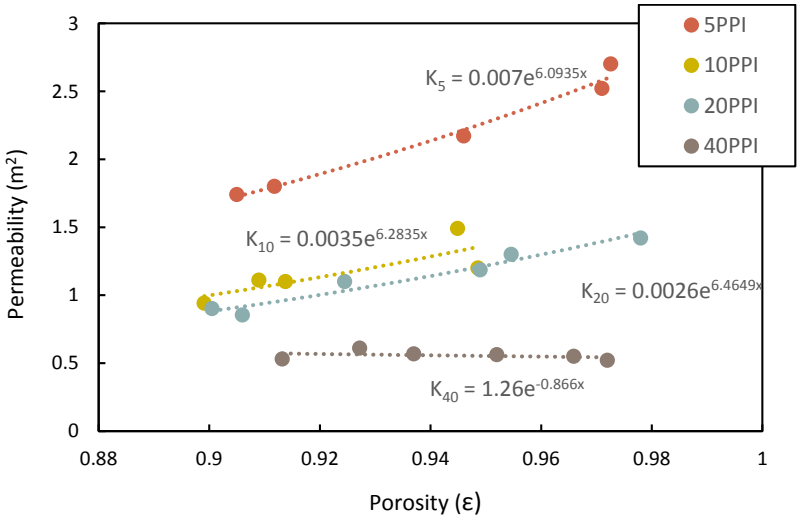

Figure 5.2. Experimental data for permeability in literature and correlation expressions.

5.2.1.2 Duplessis and Bhattacharya Model

In this work, models that include the effect of pore size as well as tortuosity are evaluated. The models developed by Duplessis et al [55] and Bhattacharya [15] are analyzed. These models differ with respect to some geometric approximation for modelling the lattice

structure. These models are compared in order to analyze which model is applicable in the current study. It is observed that the model developed by Duplessis et al has a prediction that is closer to the experimental data with respect to both, porosity and pore size. Additionally the geometry and operating conditions considered in that study are relevant to what we aim at analyzing. Hence, this model is chosen for the current study. The correlation for tortuosity by Duplessis et al is given by:

$$\chi = 2 + 2\cos\left[\frac{4\pi}{3} + \frac{1}{3}\cos^{-1}(2\varepsilon - 1)\right]. \tag{38}$$

Similarly the one developed by Bhattacharya et al is :

$$\frac{1}{\chi} = \frac{\pi}{4\varepsilon}\left\{1 - \left(1.18\sqrt{\frac{(1-\varepsilon)}{3\pi}}\frac{1}{G}\right)^2\right\}. \tag{39}$$

The permeability is then evaluated by the following relations:

$$K = \frac{\varepsilon^2 d^2}{36(\chi-1)\chi} \tag{40}$$

$$d = \sqrt{\frac{\chi}{3\varepsilon}}d_P\ . \tag{41}$$

A detailed derivation can be found in [55].The pressure drop then, can be found out using Darcy's law as:

$$-\frac{\partial P}{\partial x} = \frac{\mu}{K}u_{mod} + \frac{\rho C_E}{\sqrt{K}}u_{mod}^2 \tag{42}$$

$$u_{mod} = u_{in} \times \frac{A_{ap}}{A_f} = \frac{u_{in}}{\varepsilon}\ . \tag{43}$$

Both the viscous and inertia terms are taken into account. Figure 5.3 shows the comparison of results between experimental data from literature, the constant pores size model and the Duplessis et al model. Since the previous study was specific to 10 PPI, it is

compared with the values corresponding specific pore size from the Duplessis model. A comprehensive dependence of pore as well as porosity is shown in the subsequent Figure 5.4. Figure 5.3 is one particular curve corresponding to 0.002mm (10 PPI) from the 3D surface in Figure 5.4. A divergence from the correlation model is observed at very high porosity values.

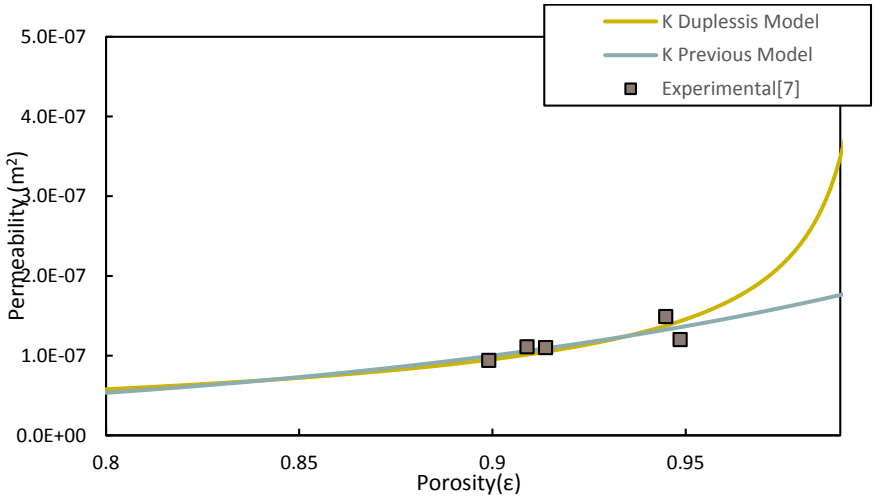

Figure 5.3. Comparison of multiple permeability models with experimental data for 10 PPI.

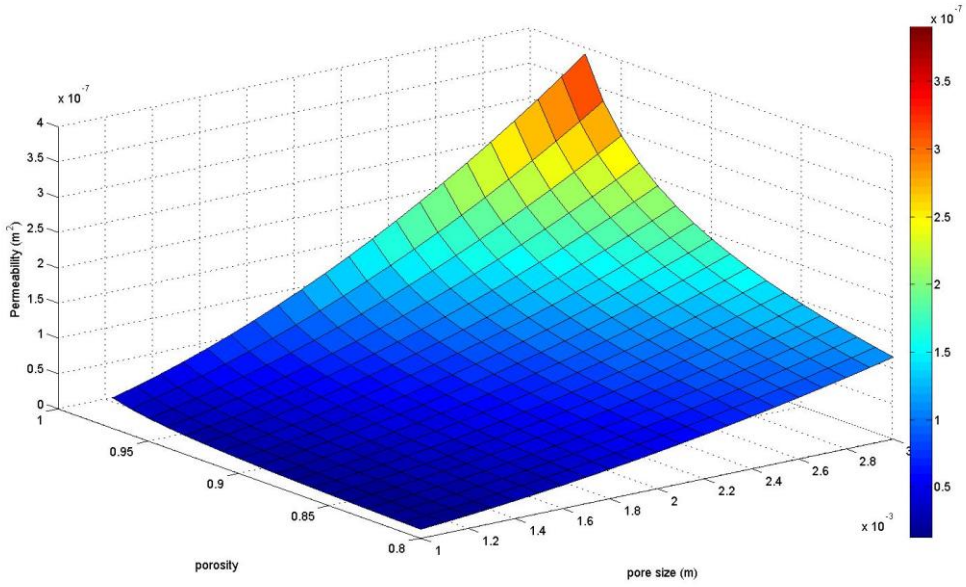

Figure 5.4. Permeability Duplessis model.

5.2.2 Reynolds Number

The Reynolds number is found from the expression of friction factor and knowledge of the pressure gradient through Darcy's equation. The friction factor is equal to the sum of inverse of the Reynolds number and the Ergun's Coefficient. This expression is empirical for the Reynolds number 'Re_k', specifically analyzed for porous mediums and is shown to hold true by Paek et al [24]. This is a standard expression used in case of porous media. For lower values of porosities the Ergun's coefficient is relatively negligible. Hence,

$$f = \frac{1}{Re_k} + C_E \approx \frac{1}{Re_k} = \frac{(-\frac{\partial P}{\partial x})\sqrt{K}}{\rho U_{mod}^2}. \quad (44)$$

This expression is widely used in numerous literatures and agrees well with the experimental work for metal foams [24],[51],[56],[57]. Reynolds number can be

calculated using the parameters- permeability, porosity and the inlet velocity, viscosity and the density of fluid:

$$\mathrm{Re_k} = \frac{\rho U_{in}\sqrt{K}}{\mu\varepsilon}. \tag{45}$$

Some of the subsequent correlations developed in this model for the heat transfer coefficients, are valid only for a small effective Reynolds number and hence the inlet velocity is chosen such that the Reynolds number lies between 0-20. The chosen velocity is 1 m/s, which is reasonable in case of standard operating conditions. Note that Reynolds number is a function of the porosity and pore size. Figure 5.6 shows this relation. The Reynolds number calculated from the Duplessis et al relationship, is characterized as an effect of both, porosity and pore size. A comparison of the correlation based model and the Duplessis permeability model is depicted in Figure 5.5.

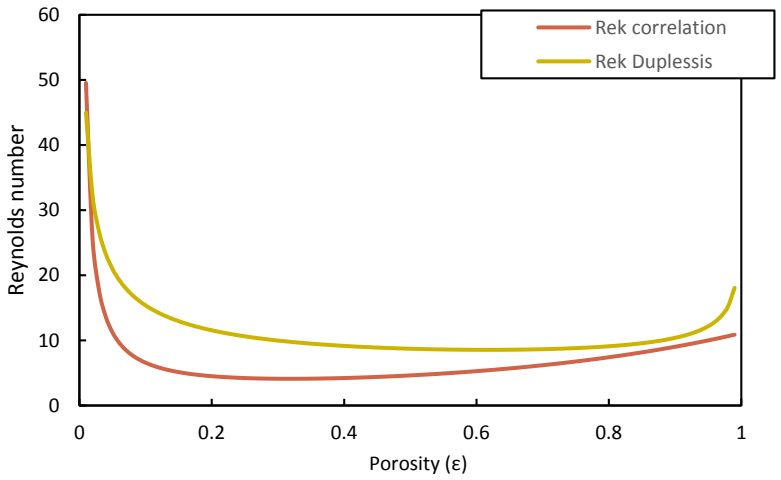

Figure 5.5. Reynolds number comparison for the two permeability models.

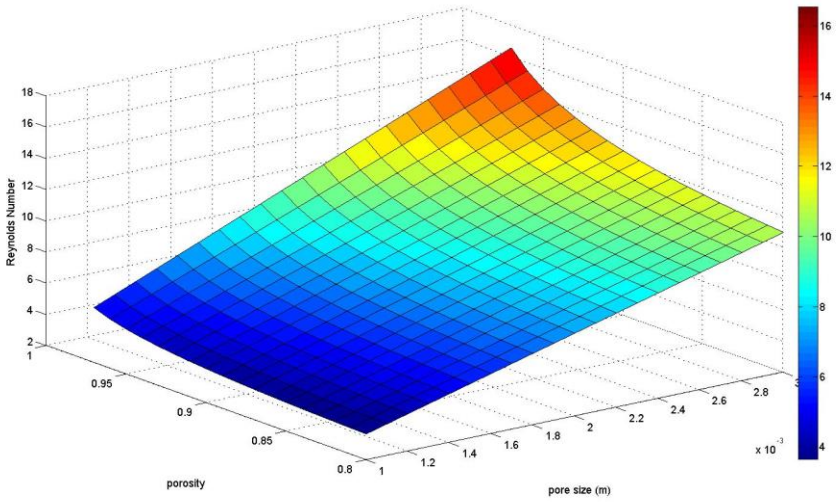

Figure 5.6. Reynolds number as a function of porosity and pore size.

5.2.3 Specific Surface Area

Specific surface area σ [m2/m3] is the surface area of fluid-solid contact per unit volume for the fluid flowing through the medium. Surface area depends on the pore density and the porosity. The surface area here actually refers to the area of contact between the fluid and the solid assuming that there are continuous flow paths and continuous solid bridges for any porosity. Zero porosity must have zero surface area and as the porosity increases, the fluid-solid contact surface area keeps increasing until reaching to a point where the solid material no longer maintain the bridges, then the surface area gradually decreases with increasing porosity. The objective is to characterize this surface area as a function of porosity and pore size. Liu [58] provides a general mathematical relationship to predict the specific surface area. The constants in the expression are determined experimentally for aluminum. The relationship is given by:

$$\sigma = \frac{C}{d_p}[(1-\varepsilon)^{\frac{1}{2}} - (1-\varepsilon)](1-\varepsilon)^{n}]. \quad (46)$$

Where, C = 281.8 and n = -0.4. Similar expressions are also developed in other studies [59]. The expression and constants change depending on the material kind and the geometry. The surface area continuously decreases with increasing pore size. But an optimum value is observed corresponding to about 0.5 of porosity.

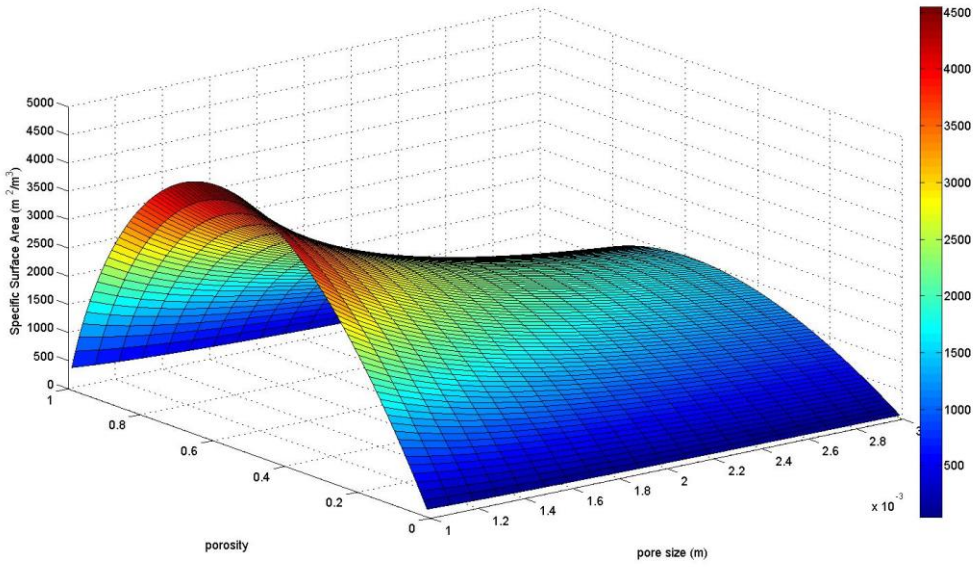

Figure 5.7. Variation of specific surface area with respect to porosity and pore size.

5.2.4 Net Heat Transfer and Temperature Distribution

The governing differential equation is determined using the energy balance. The control volume is represented in fig. Assuming a pin-fin like structure [43], the heat conduction through both the metal part and fluid part are individually evaluated by considering the effective thermal conductivity, given by:

$$-k_s A_{conds}\left.\frac{dT_{fm}}{dx}\right|_x - k_f A_{condf}\left.\frac{dT_{fm}}{dx}\right|_x = -k_s A_{conds}\left.\frac{dT_{fm}}{dx}\right|_{x+dx} - k_f A_{condf}\left.\frac{dT_{fm}}{dx}\right|_{x+dx} + h_{fm} A_{conv}(T_{fm} - T_{\infty}) \quad (47)$$

$$k_{eff} = k_s(1-\varepsilon) + k_f\varepsilon\,. \tag{48}$$

Boomsma et al [16] use the same relationship for analyzing the heat sink performance. The porous structure as a whole is then analyzed as an ordinary fin using the effective thermal conductivity, and the above governing differential equation solved. In this case analysis is carried out using the same model as [43]. The temperature for a single layer is assumed to be constant. This assumption is supported by a detailed study and experimentation in literature [43]. The cross-section areas for fluid and solid conduction perpendicular to the direction of heat conduction in the porous medium are evaluated as a function of the porosity. After applying the boundary conditions and solving the differential equations, the following relationship is obtained:

$$\theta(X) = \frac{\cosh m_{fm}(1-X)}{\cosh m_{fm}} \tag{49}$$

where, θ is dimensionless temperature and *X* is dimensionless length defined as,

$$\theta = \frac{T_{fm}-T_\infty}{T_b-T_\infty} \quad \text{and} \quad X = \frac{x}{L}\,, \tag{50}$$

$$m_{fm}^2 = \frac{h\sigma H^2}{k_s(1-\varepsilon)+k_f\varepsilon}\,. \tag{51}$$

To obtain the weighted average temperature difference for the entire medium, the function is integrated over the entire length.

$$\theta_{overall} = \int_0^1 \frac{\cosh m_{fm}(1-X)}{\cosh m_{fm}}\,dX = \frac{\tanh m_{fm}}{m_{fm}}\,. \tag{52}$$

The temperature distribution can be evaluated from the above expression if the heat transfer coefficient is known. There are multiple methods to determine the heat transfer coefficient. Kim et al [47] used a space averaging technique, wherein the heat transfer

coefficient is evaluated experimentally by knowing the operating temperatures, the inlet velocities, and the material properties. Experimentally, the heat transfer coefficient is calculated from the inlet and outlet fluid temperatures and flow rates [51][60] . A multiple-fin model has also been used to determine the performance of the porous media [61]. The number of fins in approximation depends on the porosity while the dimensions of the fins depend on the overall dimension of the medium. The overall heat transfer is evaluated for the array of fins and correlated to the heat transfer for the porous medium.

5.2.5 Heat Transfer Coefficient

5.2.5.1 Heat Transfer Correlation Model

The correlation model [4] is based on the experimental data for the heat transfer coefficient and it's variation as a function of Reynolds number. The experimental values from Bodla et al are used in this study. Additionally, Bodla et al [57] determined the heat transfer coefficient for the constant heat flux boundary in the fluid, using the governing differential equation defined by the energy balance through numerical simulations. Similar approaches exist in literatures which have similar assumptions and techniques for volume averaging. The model is limited to specific pore density. Regression curves were used to establish the correlation between heat transfer coefficient and the Reynolds number. The final expression was of the form:

$$\mathrm{h} = \alpha \mathrm{Re}_{\mathrm{K}}^{\varepsilon\beta} \quad . \tag{53}$$

Where, α = 9 and β= 0.85 for a 10 PPI foam. This correlation holds true when the Reynolds number is small. The principle being that the heat transfer is dominated by conduction at low Reynolds number whereas convection dominates at high Reynolds number. This heat transfer coefficient is an average for the entire heat sink. The relation of the heat transfer coefficient to the porosity observes a similar trend to that of the Reynolds number.

5.2.5.2 Mahajan et al Model

Additionally, another correlation developed by Mahajan et al [60] is considered. This model takes into account the effect of both porosity and pore size. The following correlations were developed empirically on the basis of experimentation for various porosity and pore size. The parameters Nu_k,Re_k Pe_k all represent the porous medium specific, permeability dependent Nusselt number, Reynolds number and Peclet number. An effective Prandtl number corresponding to the effective thermal conductivity is considered. The relationships are given by:

$$Nu_e = 6 \cdot 43 Pe_{k,e}^{3/5} \left(\frac{D_h}{d_P}\right)^{-2/3} \tag{54}$$

$$P_{e_{k,e}} = Re_k P_{r_e} \tag{55}$$

$$P_{r_e} = \frac{\mu C_P}{k_{eff}} . \tag{56}$$

The variation of the Nusselt number with respect to porosity and pore size is presented in Figure 5.9. The heat transfer coefficient is evaluated as,

$$Nu_e = \frac{h\, d_P}{k_e} . \tag{57}$$

A comparison of the heat transfer coefficient between the correlation model and Mahajan et al model is shown in Figure 5.8 .

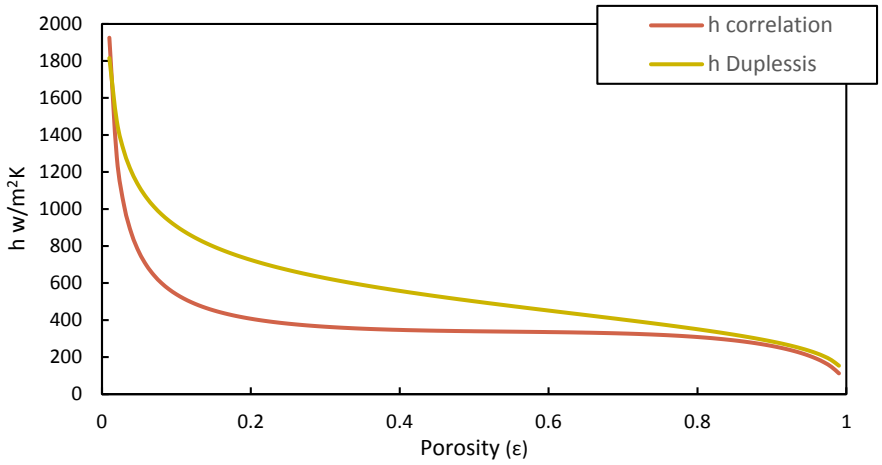

Figure 5.8. Comparison of the two models for heat transfer coefficient.

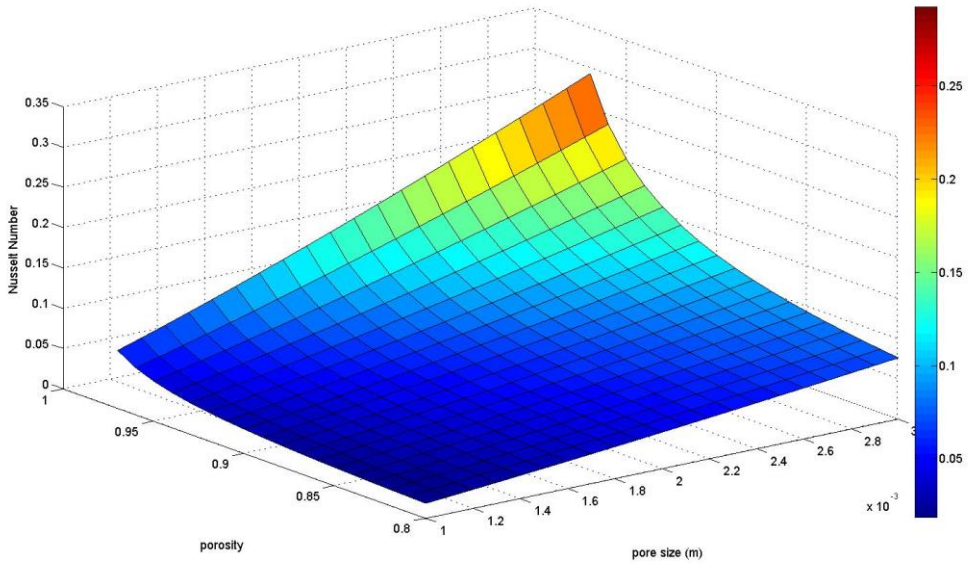

Figure 5.9. Variation of Nusselt number with respect to porosity and pore size.

As a comparison, Bhattacharya et al [15] had observed a heat transfer coefficient of about 300 W/m^{2}k for 5 PPI, 0.9 porosity sample with 1 m/s inlet velocity of air. With the current model, the prediction is 314 W/m^{2}k under the same operating conditions.

5.2.6 Pumping Work

The pumping work is defined as the work required to pump the fluid through the medium to overcome the pressure drop. The objective is minimizing the pressure drop. We evaluate the pumping work required using multiple methods and compare to find out the most appropriate model for the study. Depending on the permeability model chosen the calculated pumping work changes accordingly. An empirical relationship provided and verified in literature [22], [23] and [24] is also compared. This relationship of pumping power vs porosity was developed initially by Ergun, empirically for packed bed configurations and is considered for comparison. The actual expression is:

$$\frac{\Delta P}{L} = 150\frac{(1-\varepsilon)^2}{\varepsilon^3}\frac{\mu u}{d_P^2} + 1.75\frac{(1-\varepsilon)}{\varepsilon^3}\frac{\rho u^2}{d_P} \ . \tag{58}$$

Using the empirical models for permeability discussed above, the pumping work is evaluated as:

$$W_{pp} = \left(\frac{\mu}{K}u_{mod} + \frac{\rho C_E}{\sqrt{K}}u_{mod}^2\right) \times L \times U_{in} \times \rho_f. \tag{59}$$

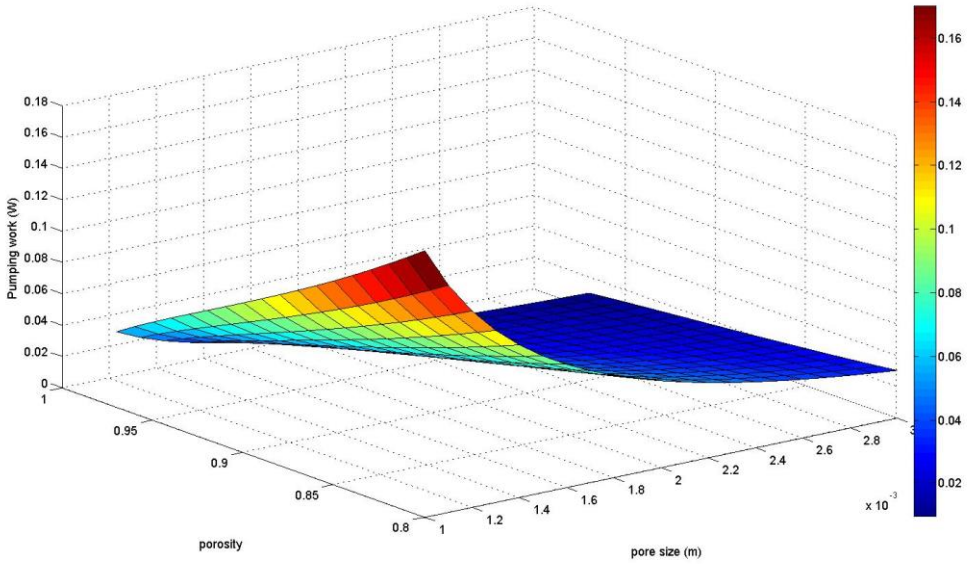

Figure 5.10. Pumping work as a function of porosity and pore size.

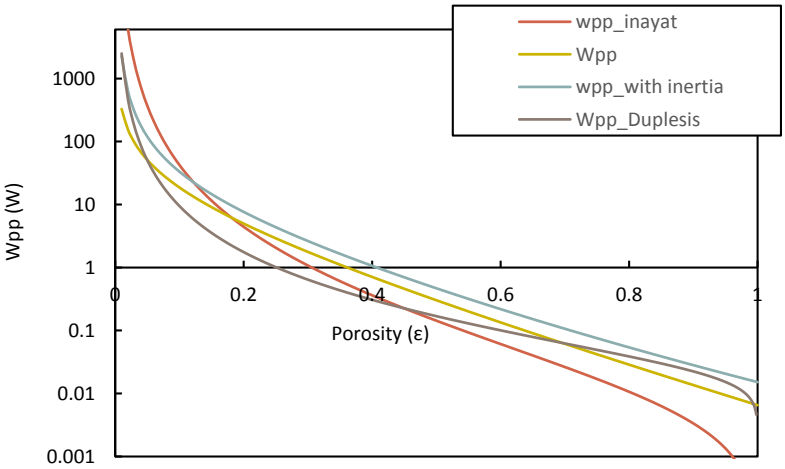

Figure 5.11. Comparison of pumping work models.

5.2.7 COP and FOM

Two parameters are defined, coefficient-of-performance (COP) and figure-of-merit (FOM) to evaluate the trade-off between the heat transfer rate and pumping work required. COP is defined as:

$$\mathrm{COP} = \frac{\mathrm{Q}}{\mathrm{W_{pp}}} \tag{60}$$

$$\mathrm{Q} = \mathrm{h} \times \mathrm{A_s} \times \theta_\mathrm{p} \times \Delta\mathrm{T}\,. \tag{61}$$

The COP is essentially a ratio of the total heat transfer rate to the pumping work required. COP can serve as an affective comparison parameter for conventional finned heat sinks and porous heat sinks for the same set of operating conditions. It is evident that the COP will be larger for larger temperature difference, but most applications have a maximum operation temperature limit and in such cases using COP to compare performance is advantageous. The design objective is then to maximize the COP. We define FOM as,

$$\mathrm{FOM} = \frac{\mathrm{Q}}{\mathrm{W_{pp}}} \times \frac{1}{(1-\varepsilon)}\ . \tag{62}$$

The FOM takes into account the effect of mass. This is relevant if the design objective is to reduce the overall weight or cost.

5.3 Results

The COP and FOM are plotted as a function of porosity and pore size in Figure 5.12 and Figure 5.13. The FOM increases exponentially with porosity as well as pore size. Hence the porosity and pore size should be as large as possible in order to maximize FOM. The maximum value of porosity is limited considering the manufacturing ability and the required mechanical strength of the foam. But the exponential trend suggests that even

a small increase in porosity results in substantial increase in FOM. Note that the value of FOM is dominated by 1/ (1-ε) and values of Q and W_{pp} have less impact. The above term causes the FOM to rise exponentially even if Q drops as A_s and θ_p decrease.

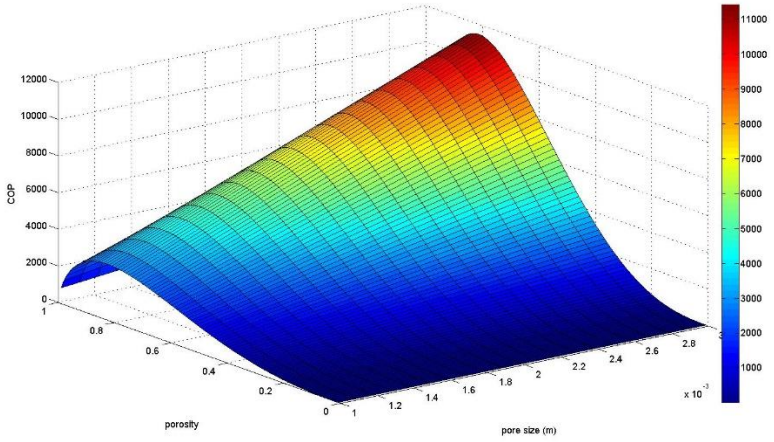

Figure 5.12. COP with respect to porosity and pore size.

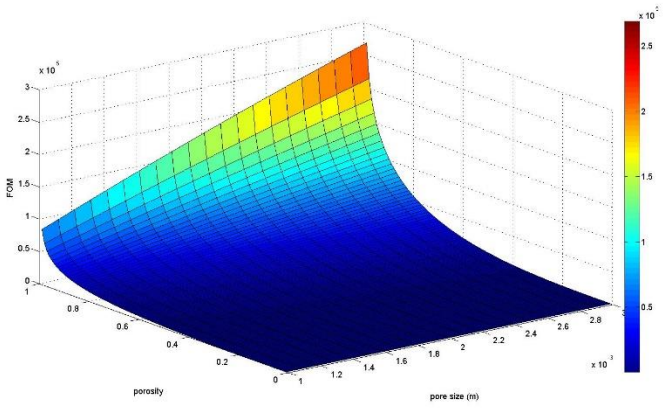

Figure 5.13. FOM with respect to porosity and pore size.

For the COP, there exists an optimum porosity corresponding to maximum COP. The optimum porosity value is observed above 0.85 for this condition. The COP increases linearly with increasing pore size. This might be explained by the fact that the pumping

work which largely affects the COP is linearly dependent with respect to the pore size. In general, the optimum value differs depending on the design, material properties, and geometric parameters. The increasing trend in the maximum COP is due to the change in pumping work and is not substantially affected by the heat transfer coefficient. This is because at low Reynolds number heat transfer by conduction dominates over convection.

5.4 Graded Porosity and Pore Size

For a uniform porous medium having constant porosity and constant pore size, it is qualitatively apparent that both pressure drop and heat transfer rate decrease with increasing porosity or pore size. For better heat transfer a smaller porosity or pore size is desirable, whereas larger porosity or pore size reduces pressure drop. A porosity or pore size graded structure aims at having smaller porosity at the base and larger porosity at the top so that the heat transfer is enhanced whereas the pumping power is reduced. A linearly and quadratic graded porosity and pore size are investigated in two individual cases.

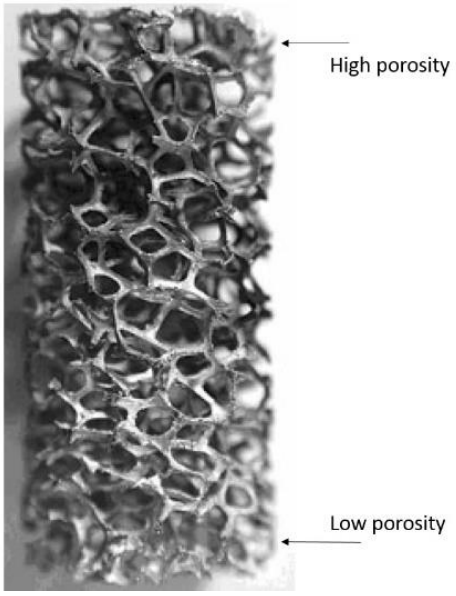

Figure 5.14. Graded porosity foam.

There are multiple methods for manufacturing graded pore and porosity structures [62][63] . It can be then useful to consider such a structure which can possibly increase the performance. The net properties, such as COP and FOM are evaluated using an averaging approach. Owing to the complicated expressions for models, the governing differential equation is solved numerically. The analysis is carried out separately for graded pore size and porosity. The effective averaged properties are evaluated for the porous structure. In the present study, we consider a linear and quadratic variation of porosity and similar variation of pore size. The variation is considered from the base (heat source side) to the top (adiabatic side), along the direction of conduction. A comparison is made to the constant property foams by considering the overall porosity and the overall pore size obtained after integrating the function over the entire length.

In case of porosity a base porosity of 0.8 was chosen and different cases were considered where the top porosity was varied from 0.85 to 0.95. Similar analysis was carried out for linear as well as quadratic variation. The overall porosity variation observed by varying these limits was 0.825 - 0.875 for linear and 0.83 - 0.9 for quadratic variation. For the graded pore size, the base pore size is fixed to 1 mm and the top porosity varies from 1.5 mm to 2.5 mm, for both linear and quadratic gradient. The pore size variation for these chosen limits was 0.12-0.17mm for linear variation and 0.13-0.2mm for quadratic variation.

For the porosity graded foams, the results are compared by computing the overall porosity of the structure and then comparing to the equivalent constant porosity. The same applies in the case of pore size. The results for porosity gradients are shown in Figure 5.15 and Figure 5.16, and for pore size gradients Figure 5.17 and Figure 5.18. It is observed that the linear variation is no better than the constant porosity foams. Similarly for the linear variation shows almost no enhancement for the COP and FOM.

In the case of quadratic variation of the porosity and pore size, a slight enhancement is observed in both the cases. This trend suggests that the properties near the base dominate the performance. Therefore, the same base porosity with a linear or quadratic variation will result in an enhanced COP and FOM.

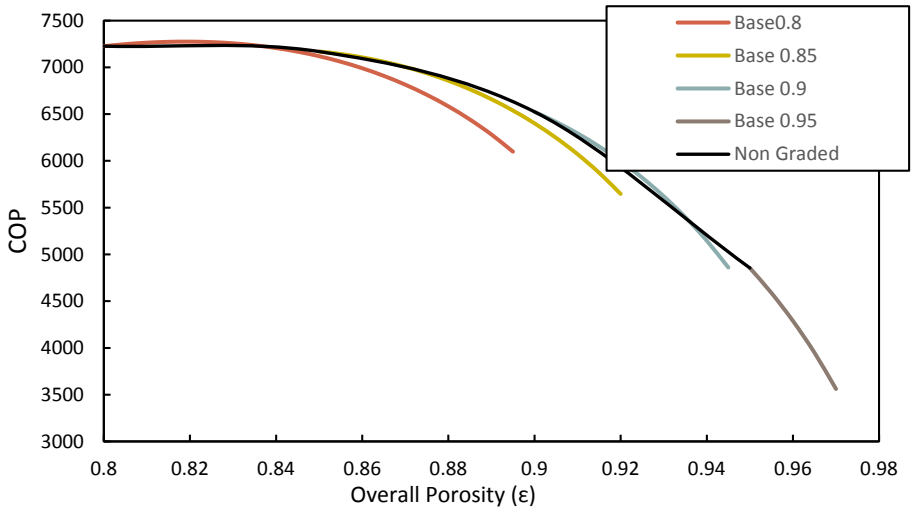

Figure 5.15. COP for graded linear porosity.

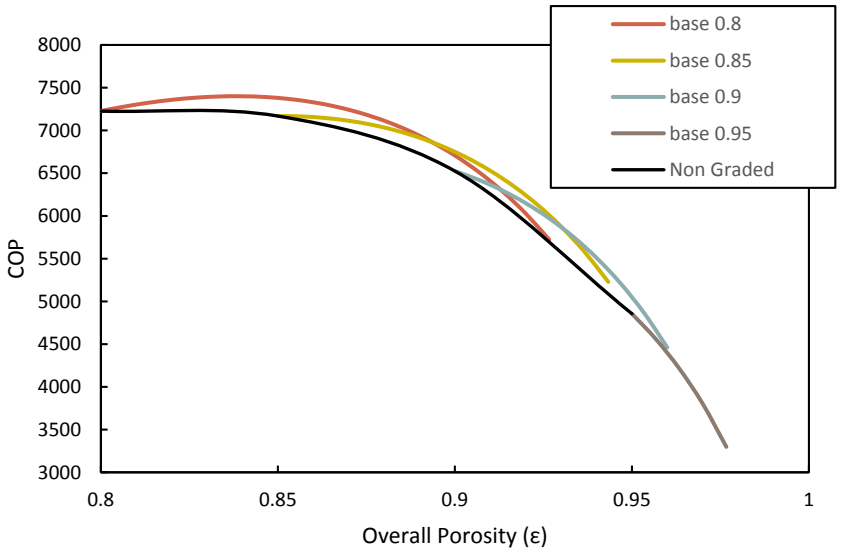

Figure 5.16. COP for grade quadratic porosity.

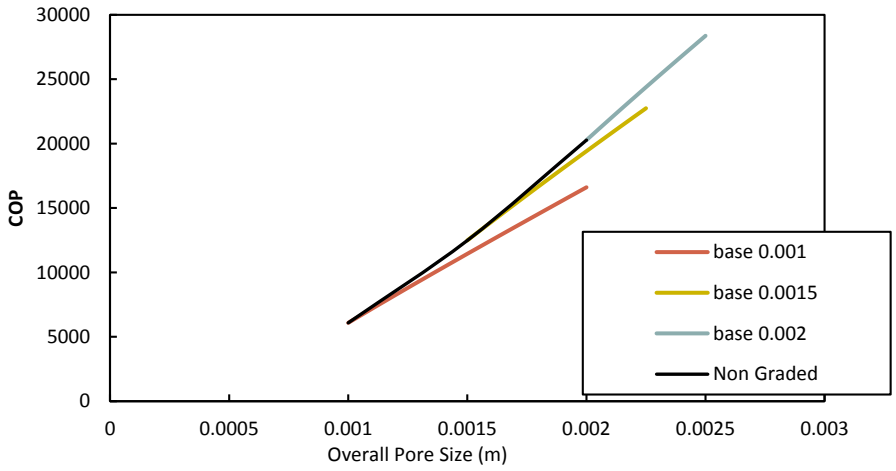

Figure 5.17. COP for graded linear pore size.

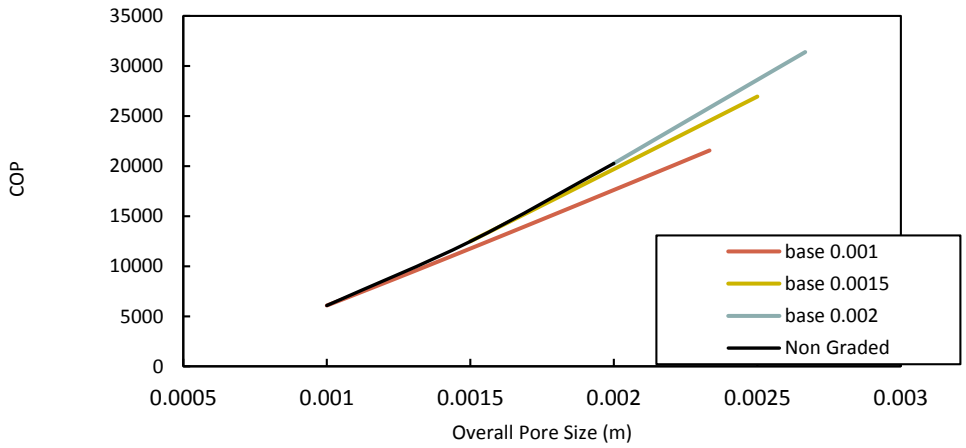

Figure 5.18. COP for graded quadratic pore size.

5.5 CFD Simulations

To better understand the flow field and temperature distribution a Computational Fluid Dynamics (CFD) analysis was done. A steady state conjugate heat transfer analysis is performed using SC/Tetra V10 and sc/STREAM software developed by SOFTWAE CRADLE. A turbulent flow SST turbulence model is used with a convergence criterion of 1e-06. The

geometry was approximated as a body-centered-cubic (BCC) void structure. This has been shown to be a valid approximation to the geometry for predicting various properties like Young's modulus, thermal conductivity, fluid flow etc. through numerical simulations and mathematical models. For our numerical investigation, three unit cell structures along the direction of the flow were considered and translational periodicity was applied at the walls. The walls were assigned a constant temperature of 320K, the inlet fluid (air), a temperature of 300K for a simplification, Figure 5.20.

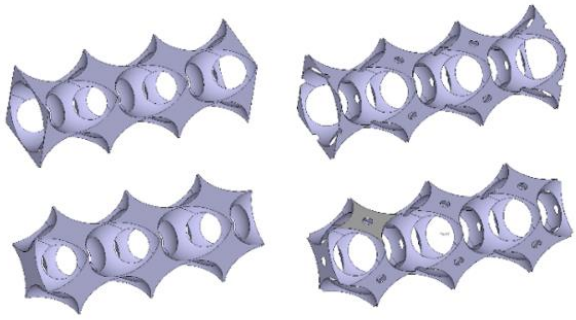

Figure 5.19. Geometries used for CFD analysis.

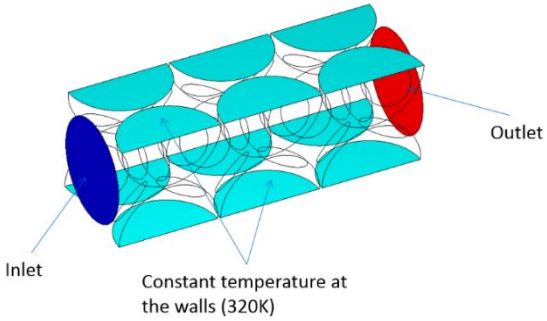

Figure 5.20. Boundary conditions for CFD analysis.

A constant static pressure was applied at the inlet (25 Pa and 12.5 Pa) and 0 Pa was applied at the outlet. The heat transfer coefficient evaluated from the outlet fluid

temperature and flow rate. An octree size between $2.5x10^{-5}$ and 10^{-4} was used. A total 3,007,858 elements and 667,560 nodes were used for the analysis.

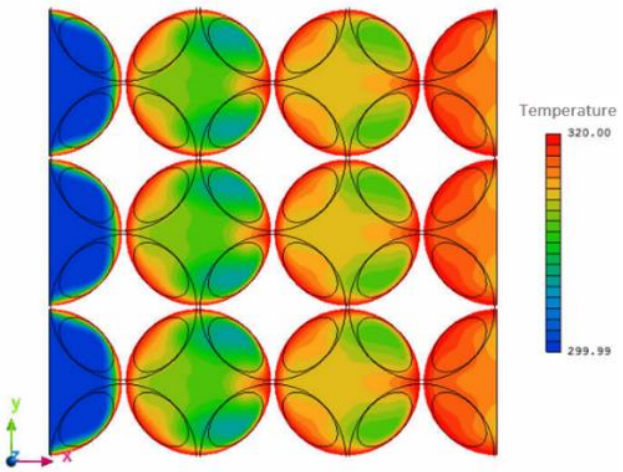

Figure 5.21. Temperature distribution from CFD simulations.

Figure 5.21 shows the flow field temperature distribution obtained from the CFD simulations. The heat transfer coefficient results were compared to the model. 0.9 porosity foams have a heat transfer coefficient of 105.92 W/m^2K through CFD whereas it was 380.2 W/m^2K in the model. For 0.95 porosity the CFD results corresponded to 219.2 W/m^2K and the model predicts heat transfer co-efficient of 315.5 W m^2K.

A discrepancy is observed in the comparison of the model and CFD simulations. The reason for this difference might be attributed to the fact that the CFD model has a constant temperature applied across the entire solid phase. The correlation on the other hand had been developed with the conditions of simultaneous conduction and convection within the medium with a constant heat flux input. The local heat transfer

coefficient is likely to change along the flow direction, which is then reflected as the difference between the calculated 'overall' heat transfer coefficients. Another factor could be the difference in the flow conditions - a constant inlet velocity condition is an assumption for the flow in the model. Whereas in the simulation a pressure difference drives the fluid flow and results in a varied flow field. This yields the result in higher velocities and higher specific Reynolds number in the model. The model predictability is diluted at higher Reynolds number. Never the less, the objective of the CFD analysis was to evaluate the flow fields and trends of the temperature variation. As observed in the local flow vectors a thin boundary layer is formed around the surface of the spherical void which has the highest temperature in the field. The thickness of this layer seems to continuously grow and decrease, hence the fresh fluid is sequentially hinting at forming and breaking of the boundary layer. This phenomenon enhances the overall heat transfer and is desirable. This can be seen from the temperature and velocity oscillations along the direction of flow probed for points at specific distances away from the surface, Figure 5.22 and Figure 5.23. This encourages future work to seek additional potential of the porous medium heat sinks.

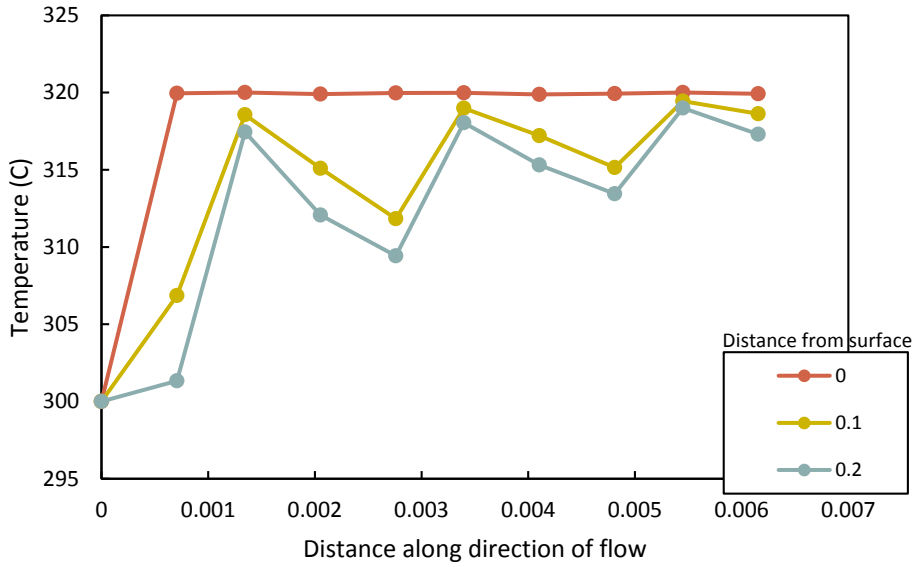

Figure 5.22. Temperature variation along flow direction for boundary layer.

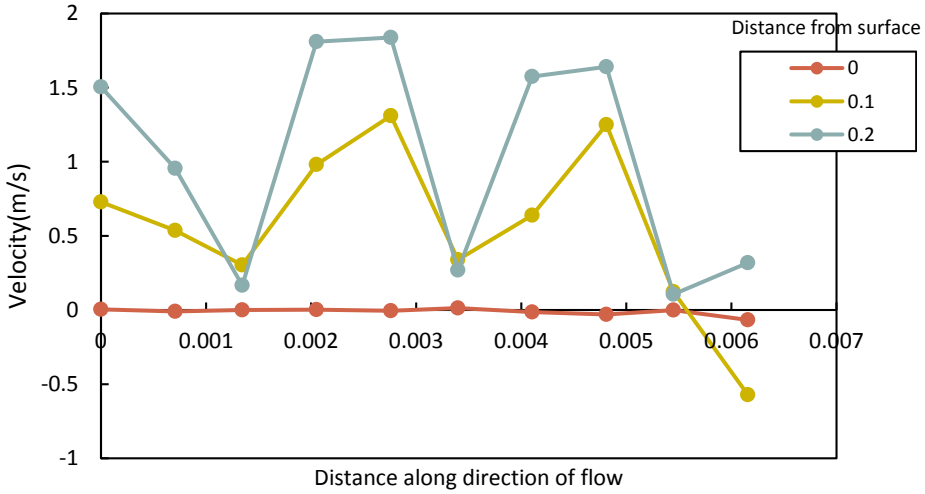

Figure 5.23. Velocity variation along flow direction for boundary layer.

CHAPTER 6. CONCLUSION

6.1 TIM

A systematic study with multiple models is provided for determining the effective thermal conductivity as a function of geometric parameters of the foam. The FEA simulations and the resistance network model provide for close predictions of experimentally observed values of effective thermal conductivity.

These models can be effectively used to predict the bulk thermal resistance of the foams. In this particular study, we used the experiments to validate the effective thermal conductivity models. These models can be effectively used to determine the bulk thermal resistance of the structure.

Analytic models have been developed to characterize the micro deformation of the foams at the surfaces. The models predict the existence of an optimum value of porosity corresponding to the maximum area of contact. The model has been generalized for the strut geometry orientation. This can accommodate for any non-ideal geometries that are created during the manufacturing process as well as help in engineering a custom structure that can have better compliance.

Experiments were performed with test setup complying with ASTM D5470 standard. The variation of the total thermal resistance with load and porosity was studied. The bulk resistance and contact resistance components were separated from the total thermal resistance. The total thermal resistance decreases with increases loads and approaches a constant value asymptotically. The trends for variation of thermal resistance with respect to porosity are coherent with what is observed in the area of contact model. There exists an optimum value of porosity which has maximum compliance and minimum thermal resistance. This value of porosity lies close to 0.95. There is a trade-off between the two components of total thermal resistance, namely, the bulk resistance and the contact resistance, which has been verified through experiments. A model for optimizing such design has been presented in this study.

As one of the approach to make the porous thermal interface for better performance relative to currently existing TIMs, additional study on use of composite materials by injecting either greases or phase change materials into the pore space may be effective. The dependence of total thermal resistance can be analyzed to obtain a bigger picture.

6.2 Heat Sink

The COP and FOM have been evaluated in the current study and for constant and graded porosity & pore size. The model has been generalized to include effect of pore size on the design. We find the optimum value of porosity lies between 0.85-0.9 which results in maximum COP. This value also depends on other parameters such as material properties

and inlet velocities. For the case of pore size, larger the pore size, better is the performance. The dependence is linear. This is attributed to the substantial drop in pumping work required by increasing the pore size. The CFD simulations help in understanding the flow trends and the heat transfer at the boundaries. These simulation techniques with the right boundary conditions can be used to verify and investigate the flow fields and temperature variations within the porous medium. The graded porosity foams show a small enhancement over constant porosity foams. Quadratic gradient is better than a linear gradient. Same is the case for pore size gradients. This analysis hints towards need for larger gradients. These could improve performance and reduce pumping power required for the same design mass of the heat sink. The model developed can be used to investigate the optimum design parameters for specific geometries and operating conditions. It can also be used to evaluate different gradients of porosity and pore size.

6.3 Practicality and Applications

The thermal resistance of these porous structures is very large as compared to the state of the art TIMs available in the industry now. In spite of this porous metal structures can have applications for low heat flux applications and TIM2. The actual application will be same as a metal pad. The application will involve installing the porous structure as in on the spreader but the entire assembly will require a clamp to hold it together. It could also be of use in applications where more robustness of the system is of essence.

Similarly for porous structure as heat sink, overcoming the high pressure drop is still a large challenge. Such porous structures can be useful for applications where low cost, low weight heat sinks are desirable. But going forward variations in the porous geometry could provide for a viable solution for even the conventional applications as a heat sink. The FOM curve gives the economic viability of such foams as a function of the porosity used. The same parameter can be used to compare conventional finned heat sinks and porous foams to appropriately determine the suitable design when optimizing in terms of weight and cost for the same performance.

As of now, the manufacturing companies prescribe the same cost for the porous structure irrespective of the porosity. But when considering large scale manufacturing the cost will be directly proportional to mass or in other words inversely proportional to the porosity. But the fact that there exists an optimum porosity for performance in both applications (TIM and heat sink) there will also exist an optimum porosity with respect to mass or cost. Figure below gives a representation of how the general trend could be like.

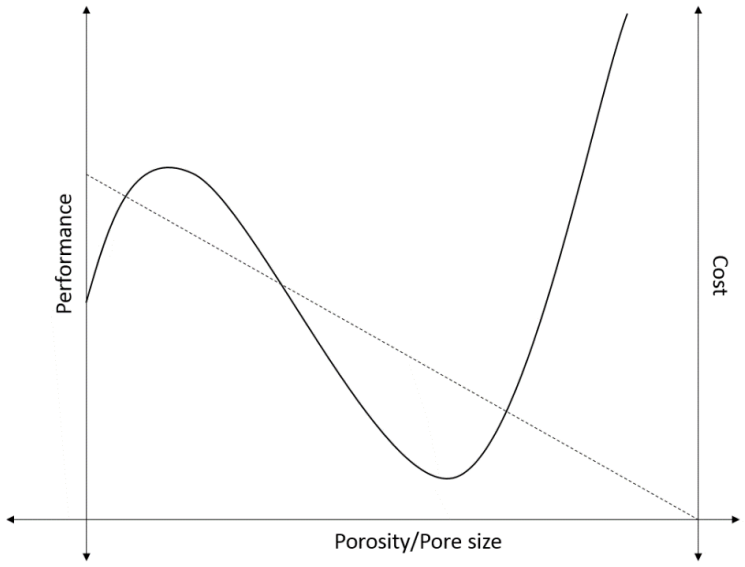

Figure 6.1. Finding the optimum value of geometric parameters with respect to cost/mass.

The actual values will depend on the operating conditions, unit cost of the material and the application in question.

6.4 The Porous Structure

The viability of the porous structure for electronics cooling applications has been targeted in this study. The models created are for generalized geometries. The current manufacturing techniques restricts the material and geometries used in these structures. The current material (aluminum) and the geometry is certainly not the best design for these applications. But going forward, with the onset of new manufacturing techniques, and use of novel materials like CNTs and graphene could provide for state of the art porous structured TIMs.

Another viable solution is to incorporate the thermal interfaces, heat spreaders and heat sinks into a single porous structure with varying porosities in all three dimensions. Such structures will not only reduce the cost but can potentially increase the overall reliability. It will also eliminate multiple contact resistances and give better control over heat transport in the three dimensions.

Currently the thermal resistance of standalone porous aluminum is substantially high in comparison to the state of the art TIMs currently used. For enhancing the conductivity, one possible direction is targeting for a large are of contact. Increasing the number of struts, geometry modifications to give maximum area of contact, geometry modification of struts on the surface, selective grinding or flattening of the edges could be possible ways to achieve a better area of contact.

Further study with respect to incorporating various gels/greases or phase change materials within the voids of the porous structure is also essential. This could provide for combined advantages of the metals pads and thermal greases.

LIST OF REFERENCES

LIST OF REFERENCES

[1] Litke, Paul, “Experimental determination of thermal contact conductance”. Purdue University Thesis, June 2002

[2] Schmidt, Aaron J., et al. "Thermal conductance and phonon transmissivity of metal–graphite interfaces." *Journal of Applied Physics* 107.10 (2010): 104907.

[3] Cross, Robert, et al. "A metallization and bonding approach for high performance carbon nanotube thermal interface materials." *Nanotechnology*21.44 (2010): 445705.

[4] Lin, Wei, et al. "Vertically aligned carbon nanotubes on copper substrates for applications as thermal interface materials: from synthesis to assembly."*Electronic Components and Technology Conference, 2009. ECTC 2009. 59th*. IEEE, 2009.

[5] Shaddock, David, et al. "Development of a compliant nanothermal interface material." *ASME 2011 Pacific Rim Technical Conference and Exhibition on Packaging and Integration of Electronic and Photonic Systems*. American Society of Mechanical Engineers, 2011.

[6] Shahil, Khan M., Vivek Goyal, and Alexander Balandin. "Thermal properties of graphene: Applications in thermal interface materials." *ECS Transactions* 35.3 (2011): 193-199.

[7] Hu, Xuejiao, Linan Jiang, and Kenneth E. Goodson. "Thermal conductance enhancement of particle-filled thermal interface materials using carbon nanotube inclusions." *Thermal and Thermomechanical Phenomena in Electronic Systems, 2004. ITHERM'04. The Ninth Intersociety Conference on*. IEEE, 2004.

[8] Xu, Yunsheng, Xiangcheng Luo, and D. D. L. Chung. "Sodium silicate based thermal interface material for high thermal contact conductance." *Journal of Electronic Packaging* 122.2 (2000): 128-131.

[9] Gao, Yunxia, and Jing Liu. "Gallium-based thermal interface material with high compliance and wettability." *Applied Physics A* 107.3 (2012): 701-708.

[10] Dinash, K., D. Mutharasu, and Y. T. Lee. "Paper study on thermal conductivity of Al 2 O 3 thin film of different thicknesses on copper substrate under different contact pressures." *Industrial Electronics and Applications (ISIEA), 2011 IEEE Symposium on*. IEEE, 2011.

[11] Gwinn, Joshua P., and R. L. Webb. "Performance and testing of thermal interface materials." *Microelectronics Journal* 34.3 (2003): 215-222.

[12] Otiaba, Kenny C., et al. "Thermal interface materials for automotive electronic control unit: Trends, technology and R&D challenges." *Microelectronics Reliability* 51.12 (2011): 2031-2043.

[13] Webb, Ralph L., and Joshua P. Gwinn. "Low melting point thermal interface material." *Thermal and Thermomechanical Phenomena in Electronic Systems, 2002. ITHERM 2002. The Eighth Intersociety Conference on*. IEEE, 2002.

[14] Singhal, Vishal, Thomas Siegmund, and Suresh V. Garimella. "Optimization of thermal interface materials for electronics cooling applications." *Components and Packaging Technologies, IEEE Transactions on* 27.2 (2004): 244-252.

[15] Bhattacharya, A., V. V. Calmidi, and R. L. Mahajan. "Thermophysical properties of high porosity metal foams." International Journal of Heat and Mass Transfer 45.5 (2002): 1017-1031.

[16] Boomsma, K., and D. Poulikakos. "On the effective thermal conductivity of a three-dimensionally structured fluid-saturated metal foam." International Journal of Heat and Mass Transfer 44.4 (2001): 827-836.

[17] Dai, Z., et al. "Correcting and extending the Boomsma–Poulikakos effective thermal conductivity model for three-dimensional, fluid-saturated metal foams."*International Communications in Heat and Mass Transfer* 37.6 (2010): 575-580.

[18] Abramenko, A. N., et al. "Determination of the thermal conductivity of foam aluminum." *Journal of engineering Physics and Thermophysics* 72.3 (1999): 369-373.

[19] Leong, K. C., and H. Y. Li. "Theoretical study of the effective thermal conductivity of graphite foam based on a unit cell model." *International Journal of Heat and Mass Transfer* 54.25 (2011): 5491-5496.

[20] Wang, Moran, and Ning Pan. "Modeling and prediction of the effective thermal conductivity of random open-cell porous foams." *International Journal of Heat and Mass Transfer* 51.5 (2008): 1325-1331.

[21] Banhart, John. "Manufacturing routes for metallic foams." *Jom* 52.12 (2000): 22-27.

[22] Baumgärtner, Frank, Isabel Duarte, and John Banhart. "Industrialization of Powder Compact Toaming Process." *Advanced Engineering Materials* 2.4 (2000): 168-174.

[23] Yang, C. C., and H. Nakae. "Foaming characteristics control during production of aluminum alloy foam." *Journal of Alloys and Compounds* 313.1 (2000): 188-191.

[24] Paek, J. W., et al. "Effective Thermal Conductivity and Permeability of Aluminum Foam Materials1." *International Journal of Thermophysics* 21.2 (2000): 453-464.

[25] Kwon, Y. W., R. E. Cooke, and C. Park. "Representative unit-cell models for open-cell metal foams with or without elastic filler." *Materials Science and Engineering: A* 343.1 (2003): 63-70.

[26] Sullivan, Roy M., Louis J. Ghosn, and Bradley A. Lerch. "A general tetrakaidecahedron model for open-celled foams." *International Journal of Solids and Structures* 45.6 (2008): 1754-1765.

[27] Zhu, H. X., J. F. Knott, and N. J. Mills. "Analysis of the elastic properties of open-cell foams with tetrakaidecahedral cells." *Journal of the Mechanics and Physics of Solids* 45.3 (1997): 319-343.

[28] Phelan, Robert, Denis Weaire, and Kenneth Brakke. "Computation of equilibrium foam structures using the Surface Evolver." *Experimental Mathematics* 4.3 (1995): 181-192.

[29] G Fourie, J., and J. P Du Plessis. "Pressure drop modelling in cellular metallic foams." *Chemical Engineering Science* 57.14 (2002): 2781-2789.

[30] Li, K., X-L. Gao, and A. K. Roy. "Micromechanics model for three-dimensional open-cell foams using a tetrakaidecahedral unit cell and Castigliano's second theorem." *Composites Science and Technology* 63.12 (2003): 1769-1781.

[31] Sihn, Sangwook, and Ajit K. Roy. "Modeling and prediction of bulk properties of open-cell carbon foam." *Journal of the Mechanics and Physics of Solids* 52.1 (2004): 167-191.

[32] Simone, A. E., and L. J. Gibson. "Effects of solid distribution on the stiffness and strength of metallic foams." *Acta Materialia* 46.6 (1998): 2139-2150.

[33] Gibson, Lorna J., and Michael F. Ashby. *Cellular solids: structure and properties*. Cambridge university press, 1999.

[34] Bart-Smith, H., J. W. Hutchinson, and A. G. Evans. "Measurement and analysis of the structural performance of cellular metal sandwich construction."*International journal of mechanical sciences* 43.8 (2001): 1945-1963.

[35] McCormack, T. M., et al. "Failure of sandwich beams with metallic foam cores."*International Journal of Solids and Structures* 38.28 (2001): 4901-4920.

[36] Chen, C., A. M. Harte, and N. A. Fleck. "The plastic collapse of sandwich beams with a metallic foam core." *International Journal of Mechanical Sciences*43.6 (2001): 1483-1506.

[37] Wicklein, M., and K. Thoma. "Numerical investigations of the elastic and plastic behaviour of an open-cell aluminium foam." *Materials Science and Engineering: A* 397.1 (2005): 391-399.

[38] Benouali, A-H., et al. "Investigation on the influence of cell shape anisotropy on the mechanical performance of closed cell aluminium foams using micro-computed tomography." *Journal of materials science* 40.22 (2005): 5801-5811.

[39] Yu, Chin-Jye, and John Banhart. "Mechanical properties of metallic foams."*Proceedings of Fraunhofer USA Metal Foam Symposium, Stanton, Delaware*. 1997.

[40] Johnson, Kenneth Langstreth, and Kenneth Langstreth Johnson. *Contact mechanics*. Cambridge university press, 1987.

[41] Singh, Ramvir, and H. S. Kasana. "Computational aspects of effective thermal conductivity of highly porous metal foams." *Applied Thermal Engineering* 24.13 (2004): 1841-1849.

[42] Bauer, T. H. "A general analytical approach toward the thermal conductivity of porous media." *International Journal of Heat and Mass Transfer* 36.17 (1993): 4181-4191.

[43] Dukhan, Nihad, et al. "One-dimensional heat transfer analysis in open-cell 10-ppi metal foam." *International Journal of Heat and Mass Transfer* 48.25 (2005): 5112-5120.

[44] Alam, M. K., A. M. Druma, and C. Druma. "Thermal transport in graphitic carbon foams." *Journal of composite materials* 38.22 (2004): 1993-2006.

[45] Maruyama, Benji, et al. "A new technique for obtaining three-dimensional structures in pitch-based carbon foams." *Scripta materialia* 54.9 (2006): 1709-1713.

[46] Krishnan, Shankar, Jayathi Y. Murthy, and Suresh V. Garimella. "Direct simulation of transport in open-cell metal foam." *Journal of heat transfer* 128.8 (2006): 793-799.

[47] Kim, Seo Young, Byung Ha Kang, and Jin-Ho Kim. "Forced convection from aluminum foam materials in an asymmetrically heated channel." *International Journal of Heat and Mass Transfer* 44.7 (2001): 1451-1454.

[48] Dias, M. R., et al. "Permeability analysis of scaffolds for bone tissue engineering." *Journal of biomechanics* 45.6 (2012): 938-944.

[49] Khayargoli, P., et al. "The impact of microstructure on the permeability of metal foams." *CSME forum*. Vol. 2004. 2004.

[50] Saar, Martin O., and Michael Manga. "Permeability-porosity relationship in vesicular basalts." *Geophysical Research Letters* 26.1 (1999): 111-114.

[51] Boomsma, K., D. Poulikakos, and F. Zwick. "Metal foams as compact high performance heat exchangers." *Mechanics of Materials* 35.12 (2003): 1161-1176.

[52] Jackson, Graham W., and David F. James. "The permeability of fibrous porous media." *The Canadian Journal of Chemical Engineering* 64.3 (1986): 364-374.

[53] Shimko, Daniel A., and Eric A. Nauman. "Development and characterization of a porous poly (methyl methacrylate) scaffold with controllable modulus and permeability." *Journal of Biomedical Materials Research Part B: Applied Biomaterials* 80.2 (2007): 360-369.

[54] Shimko, Daniel A., et al. "Effect of porosity on the fluid flow characteristics and mechanical properties of tantalum scaffolds." *Journal of Biomedical Materials Research Part B: Applied Biomaterials* 73.2 (2005): 315-324.

[55] G Fourie, J., and J. P Du Plessis. "Pressure drop modelling in cellular metallic foams." *Chemical Engineering Science* 57.14 (2002): 2781-2789.

[56] Xu, Weigang, et al. "Numerical investigation on the flow characteristics and permeability of three-dimensional reticulated foam materials." *Chemical Engineering Journal* 140.1 (2008): 562-569.

[57] Bodla, Karthik K., Jayathi Y. Murthy, and Suresh V. Garimella. "XMT-based direct simulation of flow and heat transfer through open-cell aluminum foams."*Thermal and Thermomechanical Phenomena in Electronic Systems (ITherm), 2010 12th IEEE Intersociety Conference on*. IEEE, 2010.

[58] Liu, P. S. "A new method for calculating the specific surface area of porous metal foams." *Philosophical magazine letters* 90.6 (2010): 447-453.

[59] Moreira, E. A., M. D. M. Innocentini, and J. R. Coury. "Permeability of ceramic foams to compressible and incompressible flow." *Journal of the European Ceramic Society* 24.10 (2004): 3209-3218.

[60] Bhattacharya, Anandaroop, and Roop L. Mahajan. "Finned metal foam heat sinks for electronics cooling in forced convection." *Journal of Electronic Packaging* 124.3 (2002): 155-163.

[61] Kiwan, S., and M. A. Al-Nimr. "Using porous fins for heat transfer enhancement." *Journal of heat transfer* 123.4 (2001): 790-795.

[62] Brothers, Alan H., and David C. Dunand. "Density-Graded Cellular Aluminum."*Advanced Engineering Materials* 8.9 (2006): 805-809.

[63] Hassani, Amir, Ali Habibolahzadeh, and Hassan Bafti. "Production of graded aluminum foams via powder space holder technique." *Materials & Design* 40 (2012): 510-515

APPENDICES

Appendix A: Electrolytic Iron Thermal Conductivity

Table A.1: Electrolytic iron thermal condcutivity.

Temperature (W)	Conductivity (W/mK)	Temperature (W)	Conductivity (W/mK)
2	12.32	50	163.6
3	18.48	60	149.1
4	24.62	70	134.9
5	30.76	80	123.8
6	36.88	90	115.4
7	42.97	100	108.9
8	49	150	92.7
9	55	200	86.7
10	61	250	81.5
12	72.8	300	76.4
14	84.2	400	67.5
16	95.2	500	60.2
18	105.7	600	53.6
20	115.7	700	47.49
25	137.4	800	41.96
30	153.9	900	37.12
35	164.5	1000	32.98
40	169.1	900	37.12
45	168.3	1000	32.98

Appendix B: Operating Procedure for Experimental Setup

1) Facility inspection
    a. Switch off all the power, pneumatic switches and valves.
    b. Verify calibration for load cell and thermocouples
2) Column Assembly
    a. Clean contact surfaces of heat source heat sink and flux meter with acetone
    b. Wash sample with methanol and place it between the flux meter
    c. Properly align the load column to be perpendicular to the plate on which load cell is mounted
    d. Use a TIM (either grease- omegatherm or polymer) between the contact interfaces of heat sink/ source and flux meters
    e. Ensure connections of thermocouple wires to NetDAQ data acquisition system. Connect the system to the computer through Ethernet cable
3) Loading system
    a. Carefully open main pneumatic valve, adjust pressure through regulator
    b. Flip the pneumatic switch to load the assembly
4) Cooling system
    a. Connect the chiller outlet to the bottom port on the heat sink and chiller inlet to the top of the heat sink
    b. Open the valve and start the pump

c. After few seconds start the cooler

d. Adjust set temperature to desired value

5) Heating system

a. After the temperatures on the bottom thermocouples drop below 10 degree Celsius switch on the DC power supply to start heaters

b. Adjust input power by appropriately adjusting either voltage or current

6) Test Procedure

a. Use fluke net data logger to generate .csv file

b. Run matlab code to track data and slope

c. Calculate resistance once system reaches steady state, evaluate over 300 sec period

d. Note pressure and load

e. Increase load through pressure regulator valve

f. Wait for next steady state

g. Repeat for desired load points

Appendix C: Sample Raw Thermocouple Temperature Data

Data for 40 PPI 0.5 inch sample with 7-9% relative density

Table C.1: Sample raw thermocouple temperature data.

Time	T1	T2	T3	T4	T5	T6	T7	T8
12000	62.4252	59.6906	56.9114	54.6158	5.64247	3.35339	0.91529	-0.76588
12001	62.4818	59.6593	56.9136	54.5965	5.72308	3.41397	0.800808	-0.77729
12002	62.4644	59.6843	56.8254	54.5387	5.73066	3.42493	0.849754	-0.88005
12003	62.399	59.6097	56.8177	54.5218	5.64046	3.40951	0.813513	-0.92318
12004	62.4116	59.6678	56.9161	54.5837	5.61354	3.33119	0.855238	-0.7986
12005	62.3962	59.631	56.8853	54.5004	5.59977	3.32069	0.786213	-0.91964
12006	62.4135	59.6455	56.8323	54.5701	5.65326	3.35402	0.823084	-0.83781
12007	62.3616	59.6482	56.8044	54.4868	5.68681	3.38105	0.843357	-0.87953
12008	62.3264	59.6249	56.827	54.5435	5.51822	3.24562	0.738368	-0.92959
12009	62.3236	59.6039	56.8518	54.5807	5.6138	3.23911	0.762652	-0.93279
12010	62.3629	59.6707	56.8454	54.6051	5.62371	3.37559	0.817322	-0.92611
12011	62.4133	59.6451	56.7617	54.4747	5.63603	3.30939	0.712993	-1.00346
12012	62.4428	59.6505	56.7793	54.5354	5.58755	3.24357	0.787685	-0.87653
12013	62.3735	59.5931	56.8289	54.5761	5.5848	3.29209	0.781549	-0.86562
12014	62.3771	59.6088	56.7924	54.5179	5.61585	3.29599	0.754451	-0.89619
12015	62.3864	59.6181	56.8386	54.5457	5.73493	3.39857	0.80942	-0.86521
12016	62.5099	59.7393	56.9268	54.6159	5.67991	3.40142	0.853569	-0.82784
12017	62.4788	59.7597	56.9473	54.6273	5.75034	3.45846	0.921209	-0.85988
12018	62.4674	59.7026	56.8776	54.6218	5.73409	3.3942	0.898055	-0.82462
12019	62.5284	59.7576	56.9421	54.5637	5.77848	3.46965	0.874182	-0.9176
12020	62.5523	59.7545	56.9051	54.6586	5.76464	3.46931	0.88747	-0.87312
12021	62.5576	59.7353	56.9778	54.6702	5.81479	3.52323	0.97943	-0.87043
12022	62.2902	59.5642	56.7476	54.4697	5.53181	3.31742	0.782924	-1.13699
12023	62.3921	59.6149	56.7617	54.4531	5.62239	3.35048	0.819533	-1.15895
12024	62.3505	59.6003	56.8389	54.5554	5.56525	3.28266	0.765155	-1.07209